

1 **Local and Remote Influences on the Heat Content of the**
2 **Labrador Sea: an Adjoint Sensitivity Study**

3 **Daniel C. Jones**¹, **Gael Forget**², **Bablu Sinha**³, **Simon A. Josey**³, **Emma J.D. Boland**¹,
4 **Andrew J.S. Meijers**¹, and **Emily Shuckburgh**¹

5 ¹British Antarctic Survey, Natural Environment Research Council, Cambridge, UK

6 ²Massachusetts Institute of Technology, Cambridge, MA, USA

7 ³National Oceanography Centre, Southampton, UK

8 **Key Points:**

- 9 • We use adjoint sensitivity fields to quantify possible influences on Labrador Sea heat
10 content
- 11 • We identify a basin-scale adjustment mechanism involving the West African and Eu-
12 ropean shelves
- 13 • Non-local heat fluxes can have a considerable impact on Labrador Sea heat content

Corresponding author: D. C. Jones, dannes@bas.ac.uk

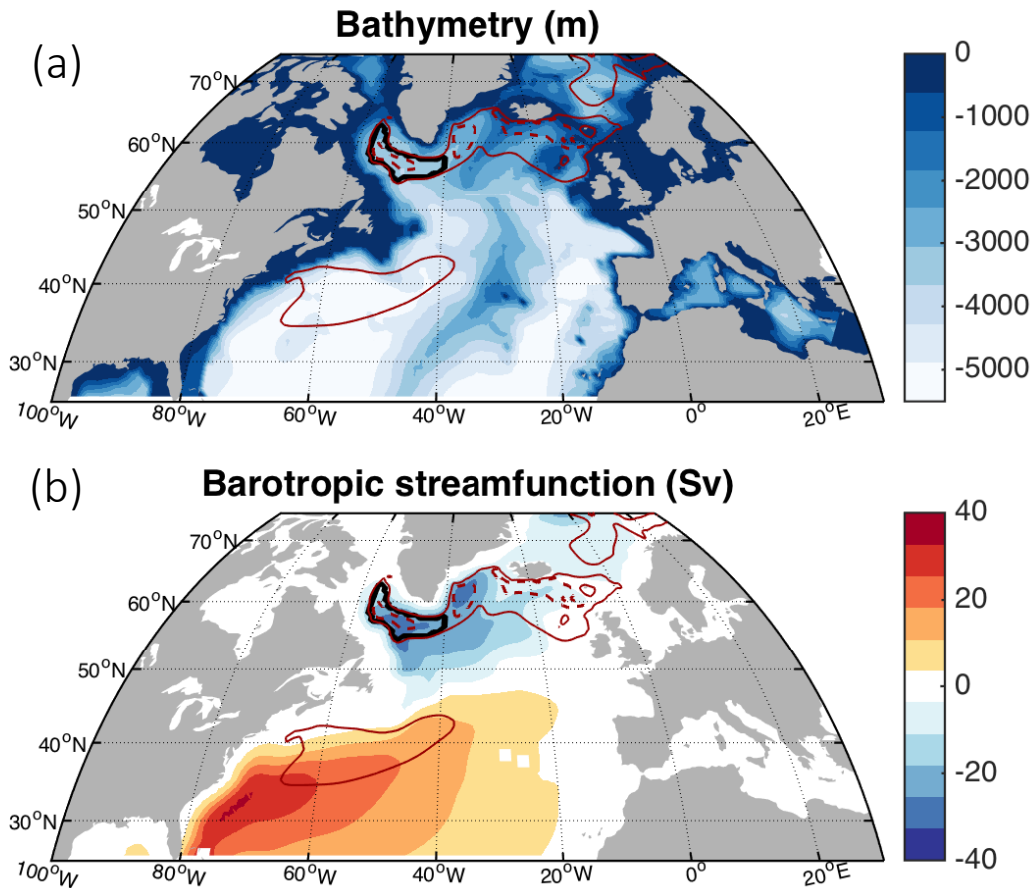
Abstract

The Labrador Sea is one of the few regions on the planet where the interior ocean can exchange heat directly with the atmosphere via strong, localized, wintertime convection, with possible implications for the state of North Atlantic climate and global surface warming. Using an observationally-constrained ocean adjoint model, we find that annual mean Labrador Sea heat content is sensitive to temperature/salinity changes (1) along potential source water pathways (e.g. the subpolar gyre, the North Atlantic Current, the Gulf Stream) and (2) along the West African and European shelves, which are not significant source water regions for the Labrador Sea. The West African coastal/shelf adjustment mechanism, which may be excited by changes in along-shelf wind stress, involves pressure anomalies that propagate along a coastal waveguide towards Greenland, changing the across-shelf pressure gradient in the North Atlantic and altering heat convergence in the Labrador Sea. We also find that non-local (in space and time) heat fluxes (e.g. in the Irminger Sea, the seas south of Iceland) can have a strong impact on Labrador Sea heat content. Understanding and predicting the state of the Labrador Sea and its potential impacts on North Atlantic climate and global surface warming will require monitoring of oceanic and atmospheric properties at remote sites in the Irminger Sea, the subpolar gyre, and along the West African and European shelf/coast system, among others.

1 Introduction

The Labrador Sea (LS) is a semi-enclosed marginal sea of the North Atlantic Ocean flanked by the continental shelves of North America and Greenland [Figure 1(a)]. Because of its partially enclosed geometry and significant seasonal buoyancy loss, the Labrador Sea features some of the deepest mixed layers in the world ocean, reaching over 2000 m in some years and in exceptional cases covering the area of the entire subpolar gyre [Lazier *et al.*, 2002; Spall, 2004; Piron *et al.*, 2017]. Temperature anomalies can enter the deep interior ocean via the Labrador Sea, potentially impacting oceanic uptake and storage of heat and carbon, with implications for global and regional climate [Pérez *et al.*, 2013; Lozier *et al.*, 2017, and references therein]. For instance, an increase in heat uptake and intermediate-depth heat storage in the subpolar North Atlantic (among other regions) during the first decade of the 21st century has been connected to a hiatus in global surface warming [Drijfhout *et al.*, 2014; Chen and Tung, 2014]. Record low densities in the Labrador Sea have been connected to reduced northward ocean heat transport and significant cooling of the upper North Atlantic

46 [Robson *et al.*, 2014, 2016]. A recent high-resolution climate model study found that such
 47 negative Labrador Sea density trends appear to be followed by positive winter states of the
 48 North Atlantic Oscillation, which can ultimately reverse the sign of the density trend through
 49 multi-decadal atmosphere-ocean interactions [Sutton *et al.*, 2017; Ortega, 2017]. Under-
 50 standing the factors that can alter Labrador Sea heat content is thus especially important for
 51 predicting the state of the North Atlantic sector and more broadly for predicting global sur-
 52 face warming.



53 **Figure 1.** ECCOv4-r2 (a) bathymetry and (b) multi-year mean barotropic streamfunction for 1992-2011,
 54 constructed from annual mean streamfunctions. The thick, solid black line indicates the Labrador Sea region
 55 wherein the March-April-May (MAM) mean mixed layer depths exceed 300 m. Also shown are the 250 m
 56 (red, solid) and 500m (red, dashed) MAM mean mixed layer depth contours for 1992-2011.

57 In addition to hosting a major pathway between the surface and interior ocean, the
 58 Labrador Sea features strong lateral circulation as it sits within the North Atlantic subpol-
 59 ar gyre that flows through the Irminger Sea from the Iceland basin to the east [Lozier *et al.*,

2017] [Figure 1(b)]. The circulation of the gyre is strongly constrained by large bathymetric features such as the Reykjanes ridge that extends southwest from Iceland and the shallow bathymetry north of the Greenland-Iceland-Scotland ridge. Components of the local circulation include the Denmark Straits Overflow and East Greenland Current that flow from the north along the eastern edge of Greenland, transporting cold fresh water from the Nordic Seas at intermediate depths and feeding into the Labrador Sea [Lozier *et al.*, 2017]. The subpolar gyre is connected to the North Atlantic Current (NAC) that flows from the Gulf Stream region to the North Atlantic, allowing influences to propagate from the subtropical gyre to higher latitudes.

Like most of the global ocean, the Labrador Sea has a long memory in that it may be affected by processes and properties in remote regions across a wide range of timescales [Robson *et al.*, 2012]. For example, changes in the nearby Irminger Sea and the remote Nordic Seas can influence stratification in the Labrador Sea [Pickart *et al.*, 2003]. Understanding how both local and remote oceanic and atmospheric properties affect the Labrador Sea is important for understanding the climate system and may help guide the design of future observational/monitoring networks [Liu and Alexander, 2007; Heimbach *et al.*, 2011]. In this study, we aim to understand how local and remote ocean properties (e.g. potential temperature) and surface forcing can affect the heat content of the Labrador Sea. We will address the following three questions:

- What are the potential source waters of the Labrador Sea?
- What are the possible influences of local and remote ocean properties on the heat content of the Labrador Sea?
- What are the possible influences of local and remote net heat fluxes and wind stresses on the heat content of the Labrador Sea?

In order to address these questions, we will use an adjoint method to calculate the linear sensitivities of the annual mean Labrador Sea heat content to the time-evolving ocean state and surface forcing. In section 2, we describe the model setup used in this paper, introduce the general concept of adjoint sensitivity experiments, and describe the particular adjoint sensitivity experiments performed in this paper. Because adjoint methods are well described in many places, we refer the reader to these works for a more thorough and general description to adjoint modeling [Thacker and Long, 1988; Marotzke *et al.*, 1999; Fukumori *et al.*, 2007; Heimbach, 2008; Mazloff *et al.*, 2010; Griewank and Walther, 2012; Verdy *et al.*, 2014,

92 for example]. In section 3, we discuss the results of our adjoint sensitivity experiments. In
93 particular, we identify and examine an adjustment mechanism that involves a teleconnection
94 between the West African shelf and the Labrador Sea. In sections 4 and 5, we summarize our
95 conclusions and offer a brief discussion on implications and possible next steps.

96 **2 Model description and experimental design**

97 We use the modeling setup associated with ECCOv4 (release 2, hereafter ECCOv4-
98 r2 or just ECCOv4), an observationally-constrained ocean state estimate, to calculate sen-
99 sitivity fields. The model setup and state estimation process are described in *Forget et al.*
100 [2015a], and the model setup is available for download on Github ([https://github.com/
101 gaelforget/ECCO_v4_r2](https://github.com/gaelforget/ECCO_v4_r2)) as an instance of the MIT general circulation model (MITgcm,
102 <http://mitgcm.org/>). ECCOv4-r2 is a product of the Estimating the Circulation and Cli-
103 mate of the Ocean (ECCO) consortium, which has produced a large variety of state estima-
104 tion products that are freely available for download via <http://www.ecco-group.org/>.
105 The adjoint model used in this work was generated using the algorithmic differentiation tool
106 TAF [*Giering and Kaminski, 1998, http://www.fastopt.com/*]. Although the state esti-
107 mation process is not the focus of this paper, for completeness we briefly describe in the next
108 section how ECCOv4-r2 was constructed. Readers interested in a more detailed description
109 are referred to *Forget et al. [2015a]*, and references therein.

110 **2.1 Description of the ECCOv4 model setup**

111 ECCOv4 uses a Lat-Lon-Cap (LLC) grid referred to as LLC90 that covers the entire
112 global ocean, including the Arctic Ocean. The horizontal grid size ranges from around 40-50
113 km in the Arctic up to 110 km at the equator. ECCOv4 solves the hydrostatic Boussinesq
114 equations *Marshall et al. [1997]* and the vector invariant form of the momentum equation on
115 the LLC90 grid [*Adcroft et al., 2004*]. The vertical coordinate is the z^* rescaled height co-
116 ordinate that redistributes changes in sea surface height throughout the entire water column
117 as opposed to changing only the uppermost grid cell [*Adcroft and Campin, 2004*]. It uses a
118 “real freshwater flux” approach [*Campin et al., 2004, 2008*] with a nonlinear free surface.
119 This method allows freshwater fluxes (with the atmosphere, land, or sea ice) to have an im-
120 pact on the model dynamics by changing the height of the free surface.

121 ECCOv4 uses a staggered time-step approach, together with Adams-Bashforth 3 (AB-
122 3) time-stepping for momentum advection, third-order Direct Space Time tracer advection
123 (DST-3; a multi-dimensional scheme), and third-order implicit tracer vertical advection (un-
124 conditionally stable) [Forget *et al.*, 2015a]. Based on the internal wave speed stability cri-
125 terion, the timestep is set to $\Delta t = 3600s$. Parameterised diffusion includes diapycnal and
126 isopycnal components, simple convective adjustment, and the GGL mixed layer turbulence
127 closure scheme [Gaspar *et al.*, 1990]. The along-isopycnal effect of unresolved eddies is pa-
128 rameterised as a bolus transport [Gent and McWilliams, 1990, hereafter GM]. In this work,
129 we use diffusivity and GM intensity parameters that have been optimized by the ECCOv4-
130 r2 state estimation process, all of which are time-invariant, three-dimensional fields [Forget
131 *et al.*, 2015b].

132 ECCOv4 features fully interactive, dynamic sea ice, so buoyancy and mass fluxes are
133 recalculated based on the thermodynamic balance of Losch *et al.* [2010]. Open ocean rain,
134 evaporation and runoff simply carry (advection through the free surface) the local SST and a
135 salinity value of zero, and runoff is provided by a monthly climatology [Fekete *et al.*, 2002].
136 Surface salinity restoring is *not* used here. Buoyancy, radiative, and mass fluxes are calcu-
137 lated using the bulk formulae of [Large and Yeager, 2009] using 6-hourly ERA-Interim re-
138 analysis fields [Dee *et al.*, 2011] as a “first guess” for the forcing fields. Specifically, we use
139 wind stress, 2 m air temperature, 2 m specific humidity, wind speed, downward longwave
140 radiation, and downward shortwave radiation as model inputs. These fields have been itera-
141 tively adjusted by the state estimation process in order to minimize model-data misfits.

142 **2.2 Validation of the ECCOv4 global ocean state estimate**

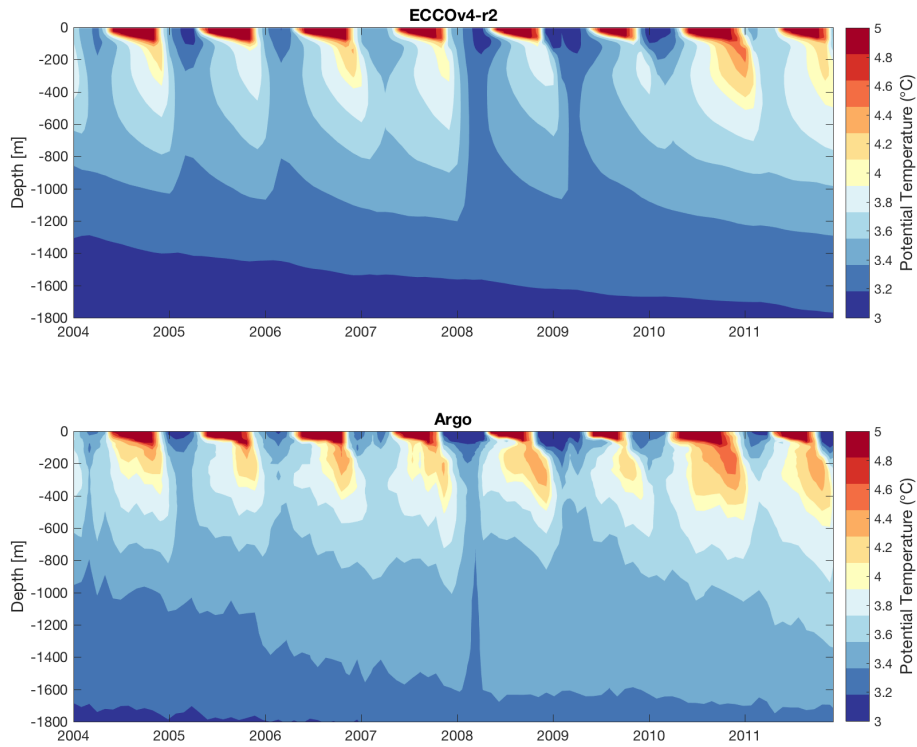
143 A perennial problem in oceanography is the paucity of observations relative to the
144 wide range of spatial and temporal scales of oceanic variability. One way to partially ad-
145 dress this data deficit is to construct a *state estimate*, in which a numerical model is brought
146 into consistency with observational data using an adjoint method [Wunsch, 2009]. In this ap-
147 proach, the initial conditions, boundary conditions (e.g. surface heat flux, wind stress), and
148 other model parameters are iteratively modified to minimize a scalar measure of model-data
149 mismatch (i.e. a *cost function*). Adjoint methods are used to calculate the sensitivity of the
150 cost function to various control parameters (e.g. initial conditions, surface fluxes), and the
151 control parameters are iteratively modified in order to minimize the model-data mismatch.
152 The result consists of both (1) an observationally-constrained estimate of the time-evolving

153 ocean state over the period covered by observations and (2) modified initial conditions, pa-
154 rameters, and boundary conditions that produce the optimised ocean state.

155 Unlike most data assimilation products, ECCOv4 does not add artificial heat, salt, etc.
156 sources and sinks in the ocean interior to fit data. Thus it is dynamically consistent in the
157 sense that the ocean state evolution (e.g. temperatures and salinities in the ocean interior)
158 remains rigorously consistent with the equations of motion and thermodynamics used in the
159 model throughout 1992-2011. Only the January 1992 initial conditions were adjusted along
160 with the optimization of diffusivity parameters and surface forcing fields in ECCOv4.

161 ECCOv4 is constrained by a global set of observations and represents the Labrador Sea
162 and more generally the North Atlantic at sufficient accuracy for our purposes. ECCOv4-r2
163 captures the annual cycle and interannual variability of Labrador Sea deep convection, as
164 seen by comparison with the gridded Argo product of [Roemmich and Gilson, 2009, RG09,
165 Figure 2]. Even though RG09 shows more high-frequency variability than ECCOv4, the two
166 products are in good agreement at seasonal and interannual time scales.

170 In Figure 3(a)-(d), we compare individual, non-gridded Argo profiles with ECCOv4
171 "profiles" taken at the locations and times of the Argo profiles in the Labrador Sea as indi-
172 cated in Figure 1. Using this approach offers a direct comparison with observations at spe-
173 cific locations and times, thus it is a particularly stringent test of the validity of the ECCOv4
174 solution. At 100 m and 750 m during the Argo period, the mean ECCOv4 temperature and
175 salinity lie within roughly 5% of the mean Argo values, although individual profiles may fea-
176 ture much larger differences (for temperatures, the 95% misfit interval is typically around
177 20% and up to roughly 50% of the Argo mean value in extreme cases). The influence of
178 deep convection from 1992-1996 can be seen in the ECCOv4 temperature and salinity pro-
179 files. ECCOv4-r2 also captures the seasonal cycle, interannual variability, and long-term
180 trend in sea level height as measured by altimetry (Figure 3(e), for more details see [Forget
181 and Ponte, 2015]). Labrador Sea bottom pressure is somewhat noisier, with a correlation
182 of approximately 0.45 between ECCOv4-r2 and the GRACE-mascons product of Watkins
183 *et al.* [2015]. ECCOv4-r2 is also in good agreement with sea surface temperatures from the
184 HadISST 1.1 product [Rayner *et al.*, 2003], with a correlation of 0.95 (Figure S1), although
185 ECCOv4-r2 sea surface temperatures are consistently colder than HadISST 1.1 in the winter.
186 Because some of the same data (e.g. Argo, altimetry) have been used to constrain ECCOv4
187 and the other products, good agreement between them is perhaps not surprising. The pre-



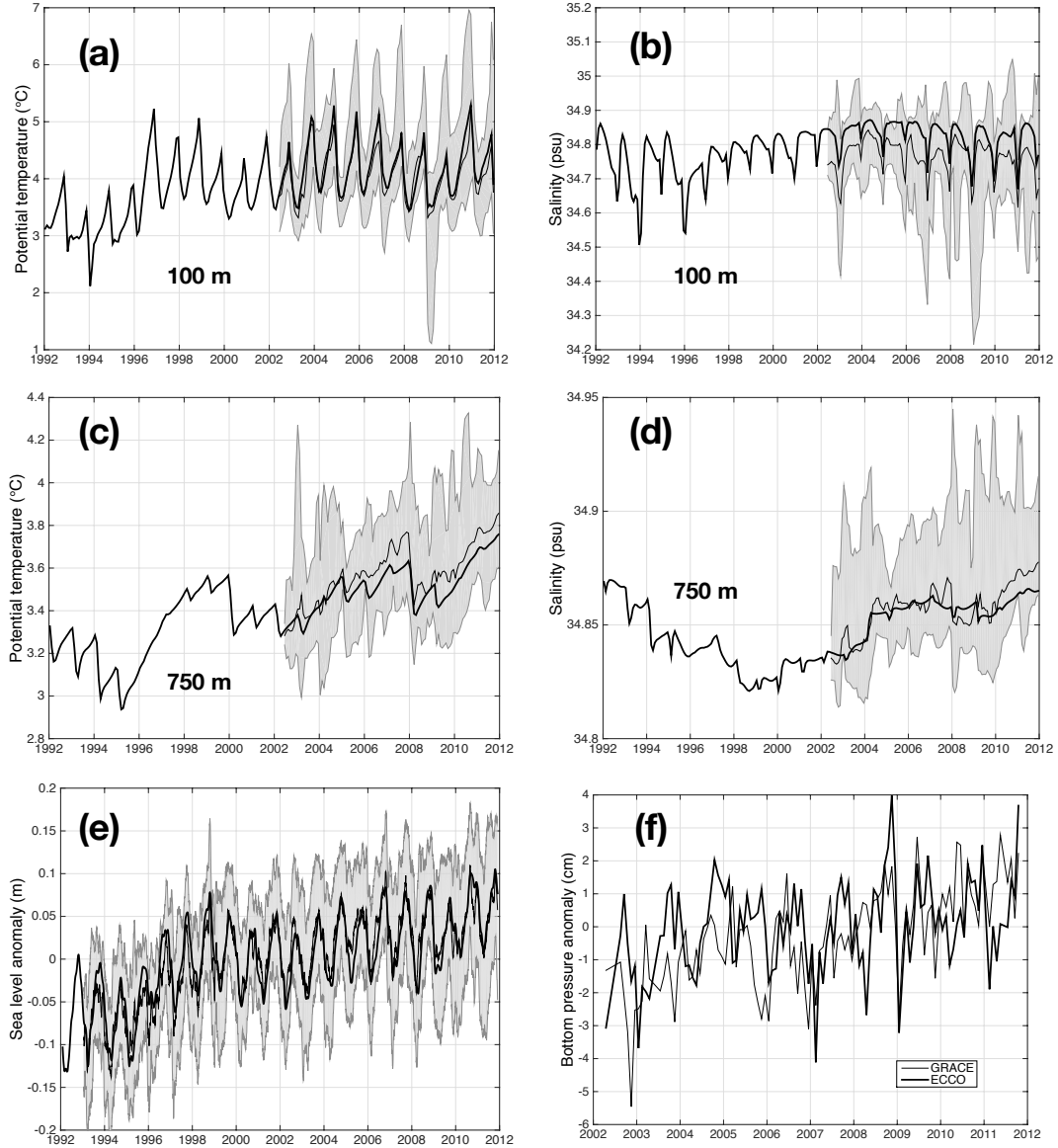
167 **Figure 2.** Comparison of ECCOV4-r2 and Argo potential temperatures (°C), averaged between 55-
168 50°W and 55-60°N. Argo data taken from Scripps gridded product [Roemmich and Gilson, 2009,
169 http://www.argo.ucsd.edu/Gridded_fields.html]

188 sented comparisons, however, provide confirmation that the Labrador Sea and the broader
189 North Atlantic are both well represented in ECCOv4-r2, giving us realistic circulation and
190 hydrography well-suited for adjoint sensitivity experiments.

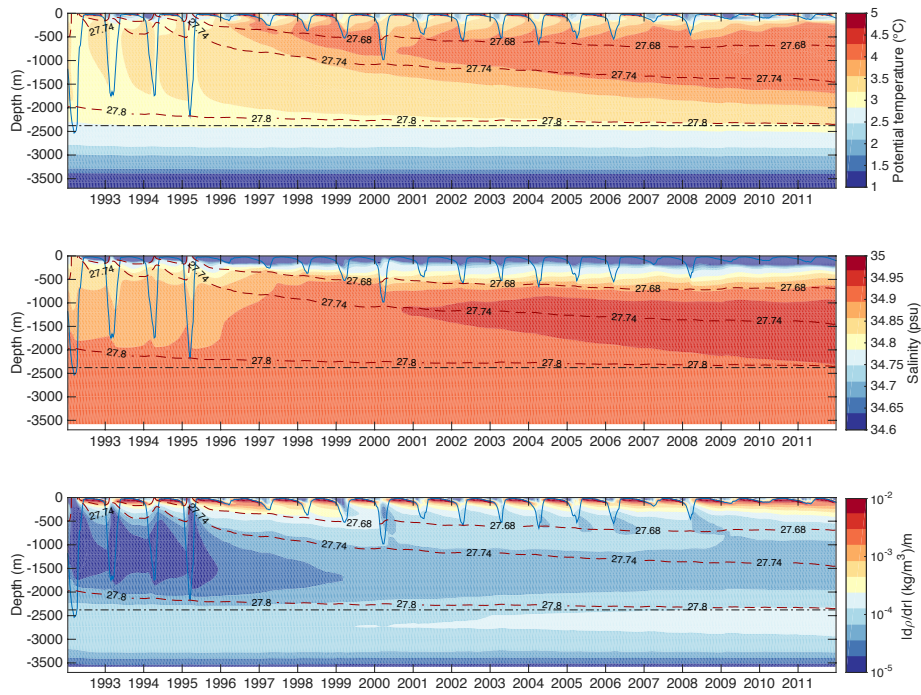
201 **2.3 Trends in the Labrador Sea in ECCOv4**

202 In the ECCOv4-r2 solution, which covers the time period 1 January 1992 to 31 De-
203 cember 2011, the Labrador Sea transitioned from a state dominated by weak stratification
204 and mixed layers reaching over 1500 m, to a more stratified state with shallower mixed layers
205 (Figure 4). The interior ocean (between roughly 100m and 2400 m) became warmer, saltier,
206 and less stratified gradually from 1996 onwards. Temperatures and salinities stayed nearly
207 constant in the deep portion of the Labrador Sea water column (below roughly 2400 m, the
208 depth of the shallowest bathymetry relative to the sea surface in the Labrador Sea as defined
209 in Figure 1), with only a slight increase in stratification. The subpolar gyre weakened over
210 this same period (Figure S2).

214 The observed changes in the Labrador Sea may be partially explained by a change in
215 the phase of the North Atlantic Oscillation (NAO) [Sutton *et al.*, 2017]. The early 1990s fea-
216 tured a positive NAO phase, with associated exceptionally cold winters leading to strong
217 preconditioning and weak stratification [Curry *et al.*, 1998; Lazier *et al.*, 2002; Latif and
218 Keenlyside, 2011; Kieke and Yashayaev, 2015]. Between 1993-1995, the mixed layer reached
219 a maximum of 2300-2400 m [Kieke and Yashayaev, 2015]. High heat loss to the atmosphere
220 produced mixed layers deeper than 2000 m and the formation of large volumes of weakly
221 stratified water as seen in ECCOv4 (Figure 4). In the late 1990s and throughout most of the
222 2000s, the NAO switched to a negative phase associated with milder winters, weaker ocean
223 heat loss, shallower mixed layers (ranging from 500-1500 m, except for 2008 and 2014, when
224 they reached 1850 m and 1700 m, respectively), and a change in the depth and density struc-
225 ture of newly formed Labrador Sea Water [Vage *et al.*, 2008; Yashayaev and Loder, 2009;
226 Sutton *et al.*, 2017]. From the late 1990s onward, the layer of dense Labrador Sea Water
227 (between $27.74\sigma_1$ and $27.8\sigma_1$) thinned as a layer of relatively shallow Labrador Sea Wa-
228 ter (between $27.68\sigma_1$ and $27.74\sigma_1$) thickened (Figure 4). The mode of Labrador Sea Wa-
229 ter that formed in the early 1990s is notable in the modern observational record [Kieke and
230 Yashayaev, 2015]. Wintertime convection in the Labrador Sea has deepened since 2012, the
231 end of the ECCOv4-r2 period, with possible implications for the formation of Labrador Sea
232 Water [Piron *et al.*, 2017; Yashayaev and Loder, 2017]. Over the historical period 1900-



191 **Figure 3.** Validation of ECCOv4-r2 with observational data in the Labrador Sea region indicated in Fig-
 192 ure 1. Comparison of ECCOv4-r2 and Argo (a),(c) temperature profiles and (b),(d) salinity profiles. Mean
 193 ECCOv4-r2 values are shown as thick black lines. Argo-ECCOv4 misfits are calculated as $m_i = (a_i - e_i) + \bar{e}_i$,
 194 where a_i is the Argo value, e_i is the corresponding ECCOv4-r2 value, and \bar{e}_i is the mean ECCOv4 value.
 195 Median values of m_i are shown as thin black lines, and the shading indicates the 95% interval for m_i , i.e.
 196 between the 2.5th and 97.5th quantiles. Comparisons are shown at 100 m and 750 m. (e) Comparison
 197 of ECCOv4 (thick black line) sea level anomaly with Topex-Poseidon-Jason family of altimeters (mean
 198 is thin black line, shading shows 95% misfit interval [Forget and Ponte, 2015]). (f) Comparison of EC-
 199 COv4 (thick black line) bottom pressure with GRACE/mascons data (thin black line), downloaded from
 200 http://grace.jpl.nasa.gov/data/get-data/jpl_global_mascons/.



211 **Figure 4.** Labrador Sea potential temperature (top), salinity (middle), and potential vorticity (bottom) in
 212 ECCOV4-r2, shown together with mixed layer depth (solid blue lines) and σ_1 density surfaces (dashed lines,
 213 units [kg/m^3]). The height of the shallowest Labrador Sea bathymetry is shown as a dashed-dotted line.

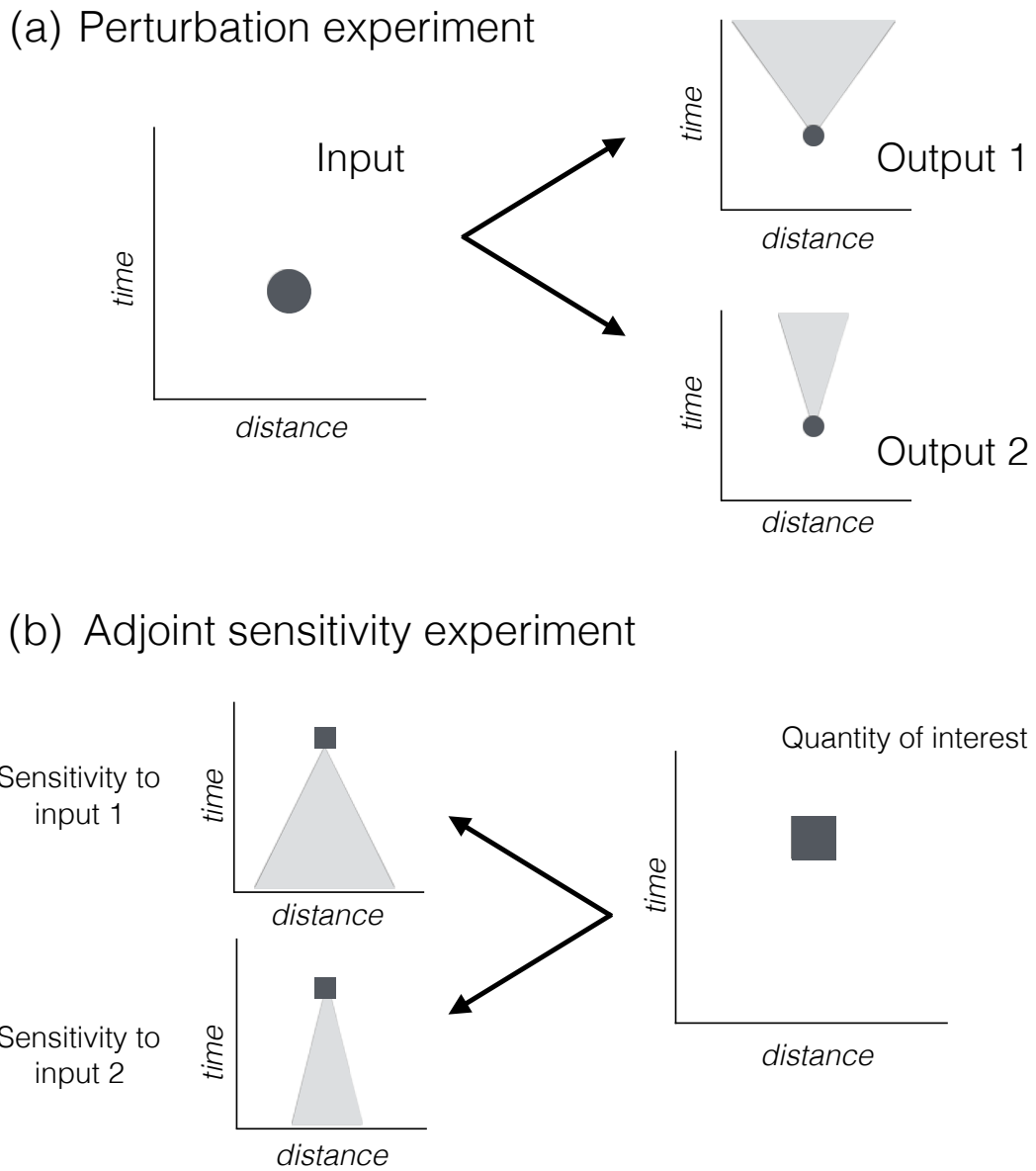
233 2000, the climatological core of deep convection was located west of 52°W and south of
234 59°N, with the deep convection area extending to 48°W and 60°N in the early 1990s and
235 retreating westward in the early 2000s [Pickart *et al.*, 2003; Vage *et al.*, 2008].

236 **2.4 Designing adjoint sensitivity experiments**

237 Adjoint methods allow for sensitivity calculations that would be extremely impractical
238 by more conventional means. In a typical “forward” perturbation experiment, the input of
239 a numerical model (e.g. net heat flux) is perturbed by a chosen finite amount at a particular
240 set of locations and times, and the effects are observed in various output fields (e.g. sea sur-
241 face temperature). The effects propagate away from the perturbation site at a range of speeds,
242 expressing the timescales of various adjustment processes. By contrast, in an adjoint sen-
243 sitivity experiment, one defines a single quantity of interest (which may be an integral over
244 some chosen region and time period), and the adjoint method simultaneously calculates the
245 sensitivities to *every* selected input at *all* locations and times that are included in the numeri-
246 cal model. Thus a single adjoint sensitivity run calculates sensitivities that would otherwise
247 require an unfeasibly large number of forward perturbation experiments.

252 One possible caveat is that adjoint sensitivities are linearized about a reference state,
253 which is a sufficiently accurate approach for some applications but not necessarily for others.
254 The linear approximation is generally expected to hold for sufficiently small perturbations
255 and short time scales. In this work, we use objective functions that are averaged over one
256 year and over the entire water column in part to ensure that the linear approximation is suit-
257 able - the response of spatially and temporally averaged objective functions tends to be more
258 linear than that of more localized and/or instantaneous quantities. The suitability of the lin-
259 ear approximation will be confirmed in section 2.4.3.

260 If we think of time in the usual way, i.e. progressing from the past to the future, then
261 adjoint sensitivity fields appear to propagate from afar, typically getting stronger with time
262 and converging on the location of interest. However, if we mentally reverse the arrow of time
263 and progress from the future into the past, then adjoint sensitivity fields appear to propagate
264 outwards from the region of interest with a range of speeds reflecting different adjustment
265 mechanisms (see Figure 5). This backwards-in-time view is convenient for interpreting ad-
266 joint sensitivity fields, as done in this paper.



248 **Figure 5.** Schematic of (a) a traditional forward perturbation experiment and (b) an adjoint sensitivity
 249 experiment. The output of the forward perturbation experiment is a set of perturbed fields (Δy), whereas the
 250 output of an adjoint sensitivity experiment is a collection of gradients (i.e. sensitivities of the form $\partial J/\partial x$,
 251 where x is an input variable.)

267 It is also worth noting that adjoint sensitivity fields are not simply correlations between
 268 variables. Adjoint sensitivity fields indicate causal relationships contained in the model
 269 equations, whereas correlations describe how two variables change together, irrespective of
 270 whether or not they are causally related. Of course, the causal relationships highlighted by
 271 adjoint methods are those of the model, which are only approximations of real processes.

272 **2.4.1 Defining the objective function**

273 First we construct an objective function (i.e. a quantity of interest) for our adjoint sen-
 274 sitivity study, which will help us (1) identify the potential source waters of the Labrador Sea
 275 and (2) understand the sensitivity of Labrador Sea heat content to local and remote forc-
 276 ing. We use a “box mean” average heat content over a control volume V and time interval
 277 $\Delta t = t_2 - t_1$:

$$J = \frac{1}{V\Delta t} \int_V \int_{\Delta t} H(\mathbf{r}, t) dt dV, \quad (1)$$

278 where H is the heat content $H = \rho_0 c_p [\theta(\mathbf{r}, t) - \theta_0]$, $\theta(\mathbf{r}, t)$ is the potential temperature, \mathbf{r}
 279 is the position vector, and t is time. The reference density is set as $\rho_0 = 1027 \text{ kg/m}^3$ and
 280 the heat capacity is $c_p = 3850 \text{ J/(kg K)}$. The reference potential temperature θ_0 is a con-
 281 stant which does not affect the sensitivities since the derivative of a constant is zero. The
 282 averaging volume V covers the entire Labrador Sea water column, delineated by the 300 m
 283 March-April-May mixed layer depth contour (averaged over 1992-2011) in the Labrador
 284 Sea as shown in Figure 1. The time integral covers a one year period from 1 January to 31
 285 December. We analyze a 10-member ensemble of 11-year adjoint sensitivity runs, with the
 286 objective function covering the last year of the run, specifically from 2002 to 2011. The en-
 287 semble approach allows us to describe the sensitivity fields in terms of ensemble means and
 288 standard deviations about the mean that reflect interannual variability over 2002-2011. Tran-
 289 sient error growth calculations suggest that ocean heat content in the North Atlantic is char-
 290 acterised by a predictability barrier of about 10 years, justifying our decision to limit our at-
 291 tention to 10-year adjoint sensitivity estimates (i.e. 10 years prior to the start of the objective
 292 function integration) [Sévellec and Fedorov, 2017].

293 **2.4.2 Using linear sensitivities**

294 Adjoint methods calculate the linear sensitivities of the objective function J to a set of
 295 independent variables x . For a selected independent variable x , an adjoint model calculates a

296 set of time-evolving sensitivity fields:

$$\frac{\partial J}{\partial x}(\mathbf{r}, t) \quad (2)$$

297 The objective function J is a scalar, but the sensitivity field $\partial_x J$ may have rich spatial and
 298 temporal structure. Throughout this work, we use 14-day averaged sensitivity fields for anal-
 299 ysis. Adjoint sensitivity fields can be scaled in various ways depending on the question at
 300 hand [Heimbach *et al.*, 2011; Verdy *et al.*, 2014]. One choice is to scale by a value of the
 301 standard deviation. For an independent variable x , we compute

$$dJ_x(\mathbf{r}, t) = \left[\frac{\partial J}{\partial x}(\mathbf{r}, t) \right] \sigma_x(\mathbf{r}), \quad (3)$$

302 where $\sigma_x(\mathbf{r})$ is the spatially-varying standard deviation in time (relative to 14-day averages)
 303 after the seasonal cycle has been removed (Figure S3). This choice means that we are us-
 304 ing an interannual standard deviation together with an annual mean objective function. Al-
 305 though this approach is expected to produce linear responses of reasonable magnitude, the
 306 spatial structure in $\sigma(\mathbf{r})$ may mask the spatial structure of the sensitivity field in a way that
 307 can make interpretation difficult. For instance, using this scaling we cannot determine if a
 308 small dJ is due to (1) weak linear sensitivity, (2) low temporal variability, or (3) a combina-
 309 tion of both. We therefore sometimes prefer to use a spatially uniform standard deviation σ_x
 310 even though it may over-represent the importance of low-variability regions in the ocean to
 311 the linear response. Still another approach is to present the sensitivity fields in their “raw”
 312 (i.e. unscaled) form, which allows a variety of scaling approaches to be applied afterwards.

313 For the purpose of plotting three-dimensional sensitivity fields (e.g. $\partial J/\partial T$), it is sen-
 314 sible to scale the sensitivity fields by the thickness of the depth level Δz . In that case, the
 315 linear response takes the form:

$$\frac{1}{\Delta z} \frac{\partial J}{\partial T}, \quad (4)$$

316 which has units of $1/m$. This scaling prevents the relatively large grid boxes in the deep
 317 ocean interior from dominating the sensitivity [Heimbach *et al.*, 2011]. In general, different
 318 approaches to scaling adjoint sensitivity patterns are appropriate for different fields and re-
 319 sponse metrics. In each section we explicitly describe the type of scaling applied for each
 320 type of analysis. Since ECCOv4 does not feature an adjoint representation of the sea ice
 321 model, sensitivities to air-sea fluxes are corrected by a factor of $1 - f$, where f is the frac-
 322 tional coverage of sea ice area in each model grid cell. For instance, the sensitivity of Labrador
 323 Sea heat content to air-sea heat fluxes in a completely ice-covered grid cell ($f = 1$) is set to
 324 zero ($1 - f$).

2.4.3 Examining the validity of the linearity approximation

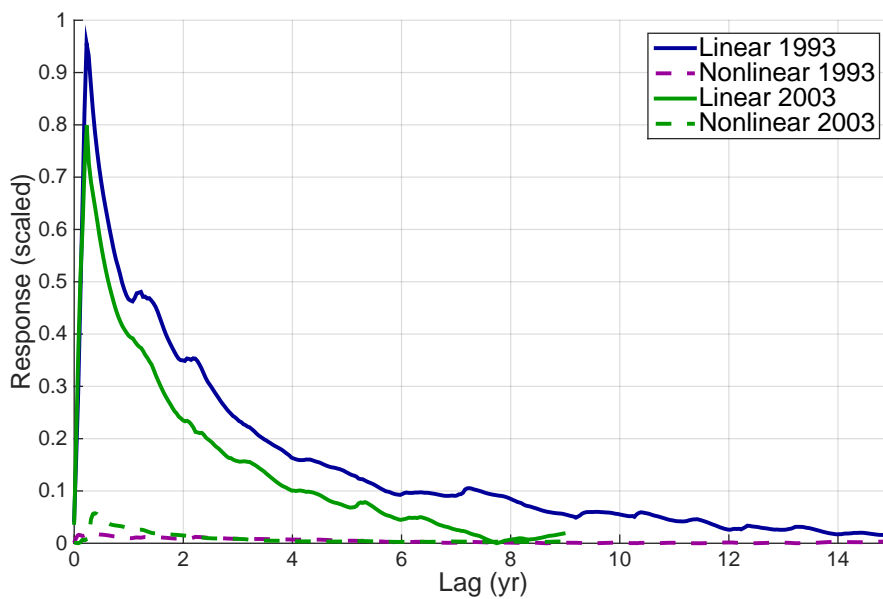
Here we test the accuracy of the linear approximation for “typical” perturbation sizes using the forward, nonlinear ECCOv4-r2 model setup. To this end, we separate the linear and non-linear responses of a given quantity by imposing positive and negative perturbations of the same magnitude in two different model runs [Verdy *et al.*, 2014]. Given a perturbation $\Delta Q = Q - Q_0$, in a quantity Q , then the response of a variable H can be approximated by Taylor series expansions as:

$$\Delta H = H - H_0 = \frac{\partial H}{\partial Q}(Q - Q_0) + \frac{1}{2} \frac{\partial^2 H}{\partial Q^2}(Q - Q_0)^2 + \dots, \quad (5)$$

where H_0 and Q_0 are reference values about which the partial derivatives are evaluated. We denote the response to a positive perturbation $Q > Q_0$ as ΔH_+ and the response to a negative perturbation $Q < Q_0$ as ΔH_- . We then estimate the linear response by the difference $(\Delta H_+ - \Delta H_-)/2 \approx (\partial_Q H)(Q - Q_0)$ and the non-linear response by the sum $(\Delta H_+ + \Delta H_-)/2 \approx 0.5(\partial_{QQ} H)(Q - Q_0)^2$. This approach is expected to work well if the response function in question can be well represented by a Taylor series expansion and if the first two non-constant terms capture the majority of the variability of that response function.

We impose positive and negative perturbations of magnitude 10 W/m² and 40 W/m² over the Labrador Sea for the first three months (JFM) of both 1993 and 2003, a total of four different perturbation experiments. We chose these years because they represent end members for the stratification of the background state and deep convection, as 1993 features exceptionally weak stratification and deep mixing, while 2003 features relatively strong stratification and a relatively shallow winter mixed layer. Using 1993 and 2003 also allowed us to run the perturbation experiments for at least 9 years and exploit almost all of the ECCOv4 period (1993-2011). When scaled by the magnitude of the perturbations (i.e. 10 and 40 W/m²), we find that the linear component of the response behaves nearly identically for both perturbation magnitudes, suggesting a high degree of linearity with respect to the magnitude of the perturbation, at least in the 10-40 W/m² range (Figure 6). In all cases, the non-linear component of the response is small, becoming significant only when the total response itself becomes negligible. For the perturbations applied in 1993, the non-linear response is small for at least 10-11 years, and for the perturbations applied in 2003 the linear response dominates for about 7 years, after which time the total response is small. Based on these results, we conclude that the linear approximation is suitably accurate on timescales of roughly 7 years for the problem of response to local air-sea heat flux. Notably, the responses show sig-

356 nificant differences when comparing 1993 and 2003, suggesting that the ocean/climate back-
 357 ground state does affect the sensitivity of the column-integrated heat content to net heat flux
 358 at the surface. In 1993, the potential temperature anomaly created by the change in heat flux
 359 penetrates much further into the interior ocean (down to roughly 2000 m) due to deep con-
 360 vection. In 2003, the potential temperature anomaly induced by the perturbation stays con-
 361 fined to a relatively narrow depth range (roughly between 0-800 m). This contrast in mixed
 362 layer depth is consistent with the behavior of the observed ocean, in that heat loss of similar
 363 magnitudes can still lead to dramatically different mixed layers, highlighting the importance
 364 of preconditioning and stratification for deep mixing [Piron *et al.*, 2017].



365 **Figure 6.** Normalized linear (solid lines) and non-linear (dashed lines) responses of the depth-integrated
 366 potential temperature of the Labrador Sea to perturbations in net heat flux. The perturbations are applied over
 367 the entire Labrador Sea with magnitude 10 W/m^2 (not shown) and 40 W/m^2 (shown) in both 1993 (blue) and
 368 2003 (green). When scaled by the magnitude of the heat flux perturbations, responses to the 10 W/m^2 and 40
 369 W/m^2 are very nearly identical.

370 **3 Results: adjoint pathways and processes**

371 In this section, we examine sensitivity fields from a 10-member ensemble of 11-year
 372 adjoint sensitivity experiments, with one experiment for each objective function year in the
 373 2002-2011 range, in order to quantify the predicted response of the Labrador Sea heat con-

374 tent to local and remote influences. We begin by decomposing the sensitivity fields into
 375 kinematic and dynamic components following *Marotzke et al.* [1999]. This allows us to dis-
 376 tinguish between sensitivities to changes that propagate along isopycnals (i.e. kinematic)
 377 with sensitivities to changing density structures (i.e. dynamic). Formulating the annual- and
 378 volume-mean heat content as a function of density and temperature $J = J[\rho(T, S), T]$ allows
 379 us to write the sensitivity of the heat content to temperature variations at constant salinity as
 380 follows:

$$\left(\frac{\partial J}{\partial T}\right)_S = \left(\frac{\partial J}{\partial \rho}\right)_T \left(\frac{\partial \rho}{\partial T}\right)_S + \left(\frac{\partial J}{\partial T}\right)_\rho. \quad (6)$$

381 The first term on the right-hand side of equation 6 is the “dynamic” component of the sensi-
 382 tivity (i.e. sensitivity to changes in density), and the second term on the right-hand side is the
 383 “kinematic” component (i.e. dynamically-inactive sensitivities to temperature anomalies).

384 Using the coefficient of thermal expansion α and coefficient of haline contraction β , defined
 385 as

$$\alpha \equiv -\frac{1}{\rho} \left(\frac{\partial \rho}{\partial T}\right)_S \quad \text{and} \quad \beta \equiv \frac{1}{\rho} \left(\frac{\partial \rho}{\partial S}\right)_T, \quad (7)$$

386 we can write

$$\left(\frac{\partial J}{\partial S}\right)_T = \left(\frac{\partial J}{\partial \rho}\right)_T \left(\frac{\partial \rho}{\partial S}\right)_T = \beta \rho \left(\frac{\partial J}{\partial \rho}\right)_T, \quad (8)$$

387 and the dynamic sensitivity becomes:

$$F_{dyn} = \left(\frac{\partial J}{\partial \rho}\right)_T \left(\frac{\partial \rho}{\partial T}\right)_S = \frac{1}{\beta \rho} \left(\frac{\partial J}{\partial S}\right)_T \left(\frac{\partial \rho}{\partial T}\right)_S = -\frac{\alpha}{\beta} \left(\frac{\partial J}{\partial S}\right)_T. \quad (9)$$

388 The kinematic sensitivity can also be written as a function of sensitivities to temperatures
 389 and salinities,

$$F_{kin} = \left(\frac{\partial J}{\partial T}\right)_S + \frac{\alpha}{\beta} \left(\frac{\partial J}{\partial S}\right)_T. \quad (10)$$

390 In these forms, the dynamic and kinematic sensitivities can be calculated directly from stan-
 391 dard MITgcm adjoint model output, which includes sensitivities to potential temperature
 392 and salinity throughout the entire model run. We use monthly 1992-2011 averaged, three-
 393 dimensional α/β fields derived from ECCOv4-r2 potential temperatures and salinities using
 394 the TEOS-10 toolbox [*McDougall and Barker, 2011*].

395 Sensitivity fields (e.g. F_{kin}, F_{dyn} , more generally written $\partial J/\partial x$) can be converted
 396 into impacts ΔJ by multiplying by perturbations Δx , i.e. $\Delta J = (\partial J/\partial x)\Delta x$. When examin-
 397 ing kinematic and dynamic sensitivity fields, we impose unit perturbations in order to pre-
 398 serve the structure of the sensitivity fields themselves. Physically, applying a unit increase
 399 of $\Delta T = 1^\circ\text{C}$ to a dynamic sensitivity field F_{dyn} can be interpreted as instead imposing a

400 density-equivalent decrease in salinity ($\Delta S = -\Delta T\alpha/\beta$) due to the presence of the factor
 401 $-\alpha/\beta$ in equation 9. Here the phrase “density-equivalent” refers to the fact that if the condi-
 402 tion $\alpha\Delta T = -\beta\Delta S$ is satisfied, then the small perturbations ΔT and ΔS have the same impact
 403 on the density via the linear equation of state for seawater, i.e. $\rho = \rho_0(1 - \alpha\Delta T + \beta\Delta S)$.
 404 In contrast, applying a perturbation of $\Delta T = 1^\circ\text{C}$ to a kinematic sensitivity field F_{kin} can be
 405 interpreted as simultaneously imposing both a $\Delta T = 1^\circ\text{C}$ change in potential temperature
 406 and a change in salinity given by $\Delta S = \Delta T\alpha/\beta$ (see equation 10). The combination of these
 407 changes ensures that the density remains constant, i.e. the perturbation is carried out along a
 408 density surface in T/S space.

409 3.1 Sensitivity to changes at constant density

410 Positive kinematic sensitivities indicate potential “source regions” for a given control
 411 volume of interest (e.g. the Labrador Sea) by quantifying the extent to which potential tem-
 412 perature anomalies may directly get transported into the region of interest at constant density.
 413 Any selected region of the global ocean integrates influences from increasingly remote re-
 414 gions as we consider increasingly distant times in the past. Thus, the volume covered by non-
 415 zero values of kinematic sensitivity tends to increase with longer lags, reflecting the action of
 416 adjoint advection, diffusion, and mixing at constant density (Figure 7).

417 For short lags (-0.8 yr in Figure 7, right-hand column), the sensitivities are concen-
 418 trated in the Labrador Sea and the wider subpolar gyre, with varying lateral influences at
 419 different depths. In the upper 500 m, sensitivity signals propagate along the eastern coast of
 420 Greenland via the East Greenland Current and the Denmark Strait Overflow, the cold and
 421 fresh currents underneath that connect the Irminger Sea and the Nordic Seas via the Den-
 422 mark Strait. Below 500 m, the sensitivities are confined to the Irminger Sea and the Iceland
 423 Basin, as the shallow bathymetry of the Denmark Strait and the ridge to the east of Iceland
 424 prevent exchange with the Nordic Seas. At lag -3.9 yr (Figure 7, middle column), the influ-
 425 ence of the subpolar gyre is apparent from the surface down to roughly 1000 m. The imprint
 426 of the North Atlantic Current is especially visible at 477 m. At lag -7.9 years, we find sensi-
 427 tivities in the Gulf Stream concentrated in the upper 900 m. At 477 m we see the broadest
 428 sensitivity pattern, with non-zero values stretching from the Gulf of Mexico to the Nordic
 429 Seas and pushing into the Arctic. In contrast, for all lags considered, the deep ocean sen-
 430 sitivities remain largely confined to the Labrador Sea and Irminger Sea, highlighting the

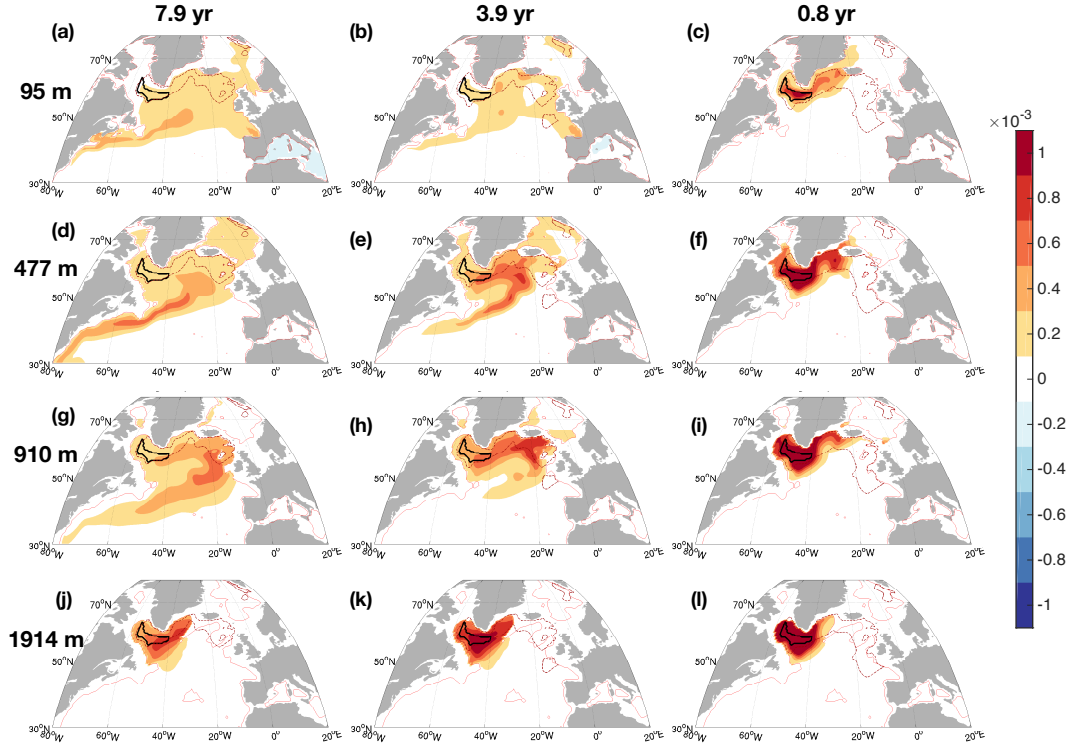
431 vastly different circulation timescales and pathways found in the upper, intermediate, and
432 deep zones of the North Atlantic.

433 Although the kinematic sensitivity field is positive nearly everywhere, we find small
434 negative sensitivities in the near-surface Mediterranean Sea (see Figure 7(a) and (b)), which
435 is a region of anomalously high salinity relative to the North Atlantic. The predicted linear
436 response of LS heat content to an increase in Mediterranean Sea temperature, together with
437 the simultaneous decrease in salinity required to keep the density constant, is a decrease in
438 LS heat content. Although this potential adjustment pathway is interesting, we do not in-
439 vestigate it further here. Animations of the kinematic sensitivity field at various depths are
440 available as supplemental information (Movie S1).

451 **3.2 Sensitivity to changes in density**

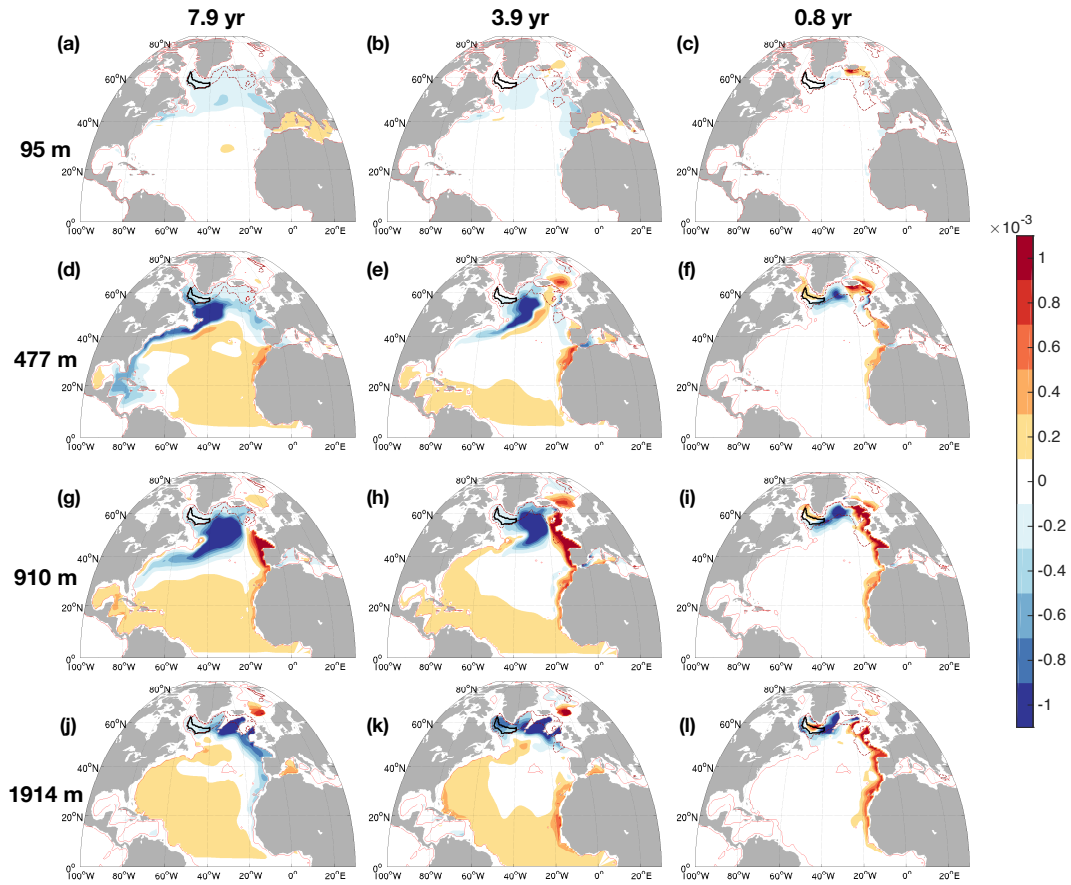
452 A change in buoyancy in any region of the global ocean can potentially influence Labrador
453 Sea heat content via re-arrangements in hydrostatic pressure fields and geostrophy, even if
454 that region is not a “source” of water for the Labrador Sea. Changes in temperature can thus
455 influence the dynamics of the ocean in various ways, for example by changing the tilt of den-
456 sity surfaces and associated geostrophic transports, and/or by exciting barotropic and baro-
457 clinic motions with characteristics similar to Kelvin waves and Rossby waves modified by
458 the presence of bottom topography. These mechanisms can potentially affect heat conver-
459 gence and thereby heat content in the LS. Like the kinematic fields, the dynamic sensitivity
460 fields are four-dimensional (three spatial dimensions, one time dimension) and thus contain a
461 tremendous amount of information.

462 At short lags (-0.8 yr, Figure 8, right column) below 100 m, we see a positive sensitiv-
463 ity anomaly along the entire eastern boundary of the subtropical and subpolar North Atlantic,
464 extending from the coast/shelf of West Africa to the coast/shelf of Iceland. For lags longer
465 than about 5 years, the sensitivity field becomes increasingly baroclinic, with variations be-
466 tween positive and negative values with depth (Figure 8, left column). This coastal/shelf
467 sensitivity field reflects a complex superposition of mechanisms that can potentially act to
468 change the basin-wide meridional pressure gradient, thereby altering the associated circula-
469 tion and ultimately heat convergence in the LS. Even though the eastern subtropical Atlantic
470 is not a source water region for the Labrador Sea, it can influence the Labrador Sea dynam-
471 ically. The kinematic sensitivities all along the African and most of the European shelf are



441 **Figure 7.** Ensemble mean kinematic sensitivities for the annual- and column-mean heat content in the
 442 Labrador Sea, shown at three different lags (-7.9 years, -3.9 years, and -0.8 years) and at four different depth
 443 levels. The objective function is defined as an average over the entire LS water column, and these plots show
 444 cuts of the sensitivity fields at 95 m, 477 m, 910 m, and 1914 m. The fields are scaled as $\partial \theta_n J / (J_0 \Delta z)$, where
 445 J is the annual mean Labrador Sea heat content, θ_n is the potential temperature, J_0 is the ensemble mean
 446 annual heat content $7.9 \times 10^6 \text{ J/m}^3$, and Δz is the thickness of the vertical level. The fields are scaled such that
 447 in a region with sensitivity $1 \times 10^{-3} [\text{m}^\circ\text{C}]^{-1}$, a unit perturbation of $\Delta T = 1^\circ\text{C}$, together with the simultaneous
 448 salinity perturbation $\Delta S = \Delta T \alpha / \beta$ required to keep the density constant, applied over a 14-day period in a sin-
 449 gle grid cell with 1 m thickness will induce a linear perturbation in the annual mean heat content of roughly
 450 $1.3 \times 10^{-10} J_0$.

472 negligibly small compared with the sensitivities in the subpolar gyre, NAC, and Gulf Stream,
 473 but the dynamic sensitivities are relatively large.



474 **Figure 8.** Ensemble mean dynamic sensitivities for the annual- and column-mean heat content in the
 475 Labrador Sea, shown at three different lags (-7.9 years, -3.9 years, and -0.8 years) and at four different depth
 476 levels. The fields are scaled in the same fashion as Figure 7.

477 Positive-negative dipoles in the dynamic sensitivity fields can indicate locations where
 478 changes in temperature can alter stratification, the tilt of density surfaces, and the associated
 479 transport (Figure 8). The dipoles seen at 477 m and 910 m across all lags tend to straddle
 480 the regions of maximum kinematic sensitivities, both of which are broadly oriented along
 481 large-scale circulation features (e.g. the eastern edge of the subpolar gyre, the NAC, the
 482 Gulf Stream). Increasing potential temperature in the region of positive sensitivity and/or
 483 decreasing potential temperature in the region of negative sensitivity leads to an *increase* in
 484 Labrador Sea heat content by changing the transport and convergence of heat. The response
 485 of the heat content is the product of the sensitivity and an anomaly, i.e. $\Delta J = (\partial_x J)\Delta x$,

486 so to understand the sign of the response we must consider both the sign of the sensitivity
487 and the sign of the anomaly in the independent variable x . This is broadly consistent with
488 a transport-driven mechanism identified by *Williams et al.* [2015] in which an increase in
489 Labrador Sea density *enhances* overturning and produces stronger heat convergence in the
490 subpolar gyre. Heat content variability in the subpolar gyre is dominated by diffusion and
491 bolus transport, which connects increased overturning with heat convergence in the subpolar
492 gyre on monthly to interannual timescales [*Buckley et al.*, 2014]. Animations of the dynamic
493 sensitivity (Movies S2, S3, and S4), and ensemble standard deviations (Figure S4) are avail-
494 able as supplemental information.

495 **3.3 Sensitivity to changes in different regions**

496 Labrador Sea heat content is influenced by increasingly remote regions as we consider
497 more negative lags (i.e. as we look further back in time). By dividing the North Atlantic
498 and Arctic Oceans into different regions based on geographic and dynamic considerations,
499 we can quantify the timescales over which these regions can contribute to variability in the
500 Labrador Sea. In Figure 9(a), we show the 9 analysis regions that we will use for the rest
501 of this paper. Regions 1, 2, and 3 are the Labrador Sea, Irminger Sea, and broader subpolar
502 gyre (which does not include regions 1 and 2), respectively. Region 4 includes Hudson Bay,
503 Baffin Bay, and part of the Northwest Passage. Region 5 consists of the Nordic Seas, with
504 a southern boundary delineated by relatively shallow bathymetric features, and Region 6 is
505 the Arctic Ocean, which is only partially shown in the chosen map projection. The subtrop-
506 ical gyre is divided into three regions based approximately on the structure of the barotropic
507 streamfunction shown in Figure 1. Region 7 contains the Gulf Stream, the Caribbean Sea,
508 and the Gulf of Mexico, with an eastern boundary that coincides with the maximum east-
509 ward extent of the 30 Sv contour of the subpolar gyre. Region 8 is the central subtropics,
510 with a maximum eastward boundary that coincides with the 5 Sv contour of the barotropic
511 streamfunction. Region 9 includes the Eastern Subtropics and the Mediterranean Sea, so it
512 will be affected by the along-shelf propagating wave signals discussed in previous sections.
513 The boundary between region 3 and the subtropical regions (7, 8, and 9) is the 0 Sv contour
514 of the barotropic streamfunction shown in Figure 1.

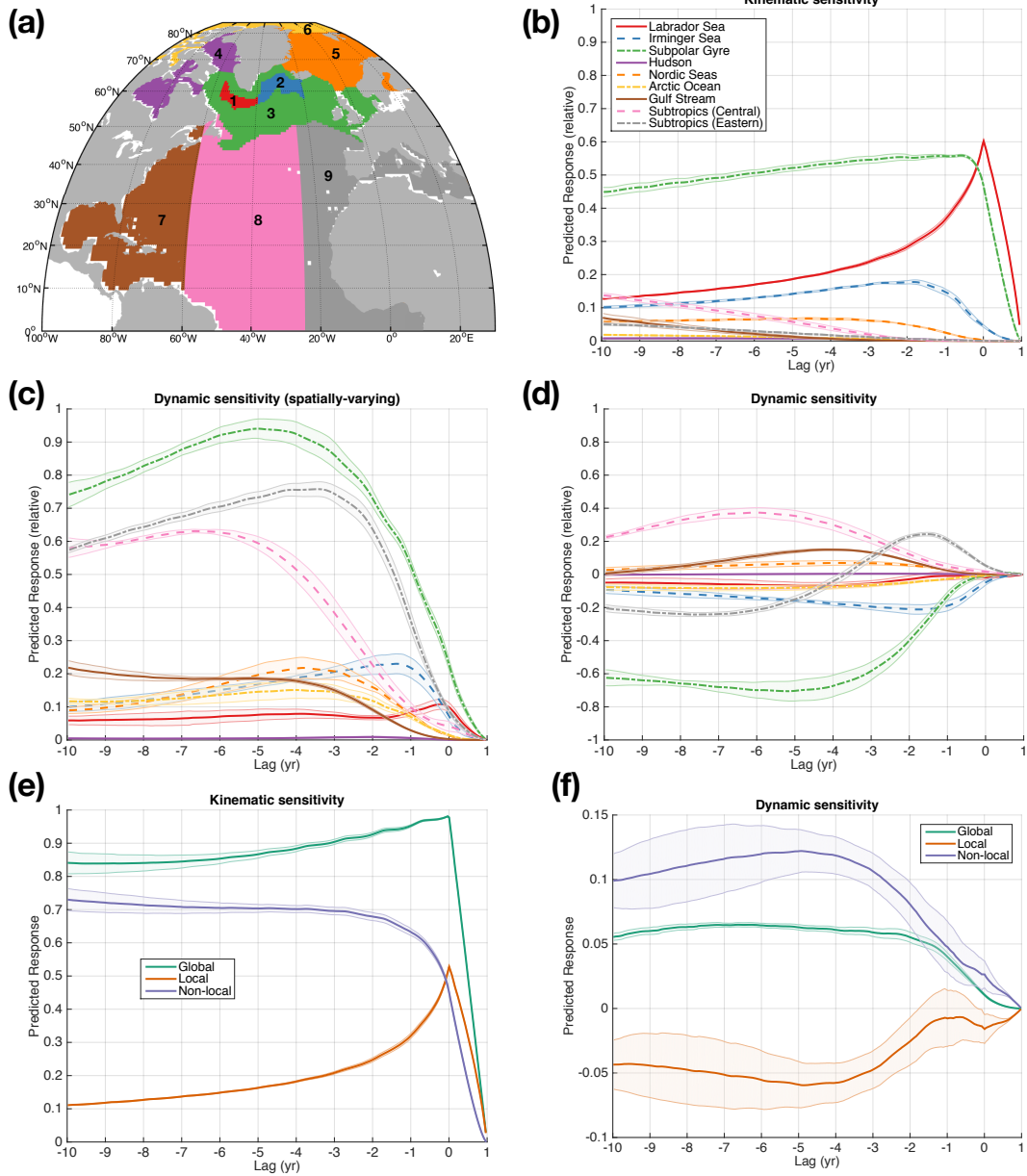
515 In each region, the response of the objective function J to a perturbation Δx at time t is
 516 generally written:

$$R_{pos}(t) = \sum_{i,j,k} \left(\frac{\partial J}{\partial x} \right)_{i,j,k,n} \Delta x, \quad (11)$$

517 where the sum is over grid cell indices within the selected region, and we choose $\Delta x = 1^\circ\text{C}$.
 518 For convenience, we will refer to this as the “pos” response, which is the response to a uni-
 519 form positive perturbation Δx . Here we use two-week averaged sensitivities, so the response
 520 function indicates the change in annual mean Labrador Sea heat content brought about by the
 521 linear response to a change in the 14-day averaged ocean state, which in this instance is taken
 522 to be a unit perturbation in potential temperature ΔT (and/or its density-equivalent perturba-
 523 tion in salinity $\Delta S = \Delta T(\alpha/\beta)$). The results are shown in Figure 9.

533 We start by analyzing the regional kinematic sensitivities. Local kinematic sensitivities
 534 (i.e. sensitivities to region 1) can be described by two-term exponential decay with a fast
 535 decay rate of 1.0 ± 0.1 yr and a slow decay rate of 12 ± 0.6 yr (ensemble mean and ensemble
 536 standard deviation). Peak sensitivity to the Irminger Sea has some spread across the model
 537 ensemble, with the maximum occurring at lag -2.1 ± 0.4 yr. Maximum sensitivity to the
 538 subpolar gyre occurs at lag -1.0 ± 0.8 yr; for longer lags it decreases roughly linearly at a
 539 rate of 1.2 ± 0.2 %/yr. The Nordic Seas sensitivity peaks at -4.7 ± 0.7 yr. The contribution of
 540 the Hudson remains negligible, probably due to its small size and its relatively inaccessible
 541 geography. On the short, 10-yr timescale of these experiments, the Arctic Ocean makes a
 542 small contribution to the response, but for lags longer than -1.8 yr, the kinematic sensitivity
 543 increases roughly linearly at a rate of 0.2 ± 0.02 %/yr.

544 The Gulf Stream region (region 7, which also includes the Gulf of Mexico) is not a
 545 major source region for the LS on 10-year timescales. In terms of the kinematic sensitivity,
 546 it reaches a relative value of 1% at lag -5.3 ± 0.4 yr. The small value of the relative contri-
 547 bution may be an artefact of the choice of region decomposition, but the time at which this
 548 maximum is reached is not sensitive to the value of the maximum. The kinematic sensitivity
 549 fields do show the imprint of the Gulf Stream at lag -7.9 yr at a depth of 477 m in Figure 7,
 550 although by this time the core of the sensitivity has not yet reached the Gulf Stream itself, as
 551 it is still located in the range of the NAC. The central subtropics shows zero sensitivity for
 552 lags shorter than -2 yr, and going further back in time it increases at a rate of 1.6 ± 0.1 %/yr.
 553 The Eastern Subtropics is not a source region for the Labrador Sea, with sensitivities well be-



524 **Figure 9.** Regional sensitivity time series for the areas indicated in panel (a). The lines indicate ensemble
 525 means, and the shading indicates the standard deviation across ensemble members. Shown are the response
 526 functions for (b) the kinematic sensitivity (R_{pos}), (c) the dynamic sensitivity (R_{var}), and (d) the dynamic
 527 sensitivity (R_{pos}). All the time series have been scaled by the same constant and so are directly comparable.
 528 Responses are total impacts of a given region, i.e. they are not scaled by the size of each region. The objective
 529 function is a year-long integral starting at lag 0. Also shown are simplified time series plots with local (i.e. in
 530 the Labrador Sea), non-local, and global (local plus non-local) predicted responses R_{pos} for the (e) kinematic
 531 sensitivity and (f) dynamic sensitivity. Note that panel (f) features a different vertical scale than the other
 532 panels.

554 low 5% for the entire 10-year experiment. For lags longer than -2 yr, the sensitivity increases
 555 at a rate of 0.4 ± 0.03 %/yr.

556 The dynamic sensitivity time series show a very different picture. We display the sen-
 557 sitivity in two different fashions. In Figure 9(d), we preserve the sign of the dynamic sensi-
 558 tivity, which can be either positive or negative; the response function is calculated as shown
 559 in equation 11, so the sign of the response of each grid cell comes from the sign of the sen-
 560 sitivity. To put it another way, equation 11 is the response to a perturbation that is uniform
 561 everywhere. As the responses are summed up in space, this approach may lead to cancella-
 562 tions within a region that contains positive and negative responses. In Figure 9(c), we instead
 563 sum up the absolute value of the dynamic sensitivity, i.e.:

$$R_{var}(t) = \sum_{i,j,k} \left| \frac{\partial J}{\partial x} \Delta x \right|_{i,j,k}, \quad (12)$$

564 where again we take $\Delta x = 1$. Conceptually, this is equivalent to performing a convolution
 565 between the sensitivity field and an anomaly field wherein the anomalies have uniform mag-
 566 nitude and the same sign as the sensitivities. As this is extremely unlikely to be realised in
 567 any particular evolution of the ocean state, one should consider the spatially-varying sensitiv-
 568 ity an upper bound (the largest possible impact, in terms of the positive/negative structure of
 569 the response).

570 The Irminger Sea displays a negative response for all lags considered, i.e. an increase
 571 in temperature here would dynamically decrease the Labrador Sea heat content. The min-
 572 imum R_{pos} occurs at lag -1.7 ± 0.3 yr, and the maximum R_{var} occurs at lag -1.6 ± 0.5
 573 yr. For the broader subpolar gyre, the extremum R_{pos} occurs at lag -6.0 ± 2.0 yr. The pre-
 574 dicted response indicates a relatively strong dynamic sensitivity to the state of the subpolar
 575 gyre in 1992 and 1993, which were years of exceptionally strong mixed layer depth and sub-
 576 polar gyre circulation within the 20-year ECCOv4 period. The Central Subtropics predicted
 577 response peaks at lag -6.1 ± 0.3 yr (R_{pos}) and lag -6.8 ± 1.2 yr (R_{var}).

578 The Nordic Seas maximum dynamic response occurs at lag -3.6 ± 0.5 yr (R_{pos}) and
 579 -3.7 ± 0.3 yr (R_{var}). The Arctic Ocean has only a weak predicted response, peaking at lag
 580 -7.1 ± 1.3 yr (R_{pos}) and -5.2 ± 2.5 yr (R_{var}). As discussed above, the Eastern Subtropics
 581 impact the sensitivity via dynamics, although it is not a strong source region for the Labrador
 582 Sea. The R_{pos} peak occurs at lag -1.5 ± 0.1 yr, whereas the R_{var} peak occurs at lag $-3.6 \pm$
 583 0.4 yr. This contrast indicates that there are cancellations that may occur when the dynamic

584 sensitivity is forced uniformly. Note that these timescales represent the total effect of many
 585 different processes,

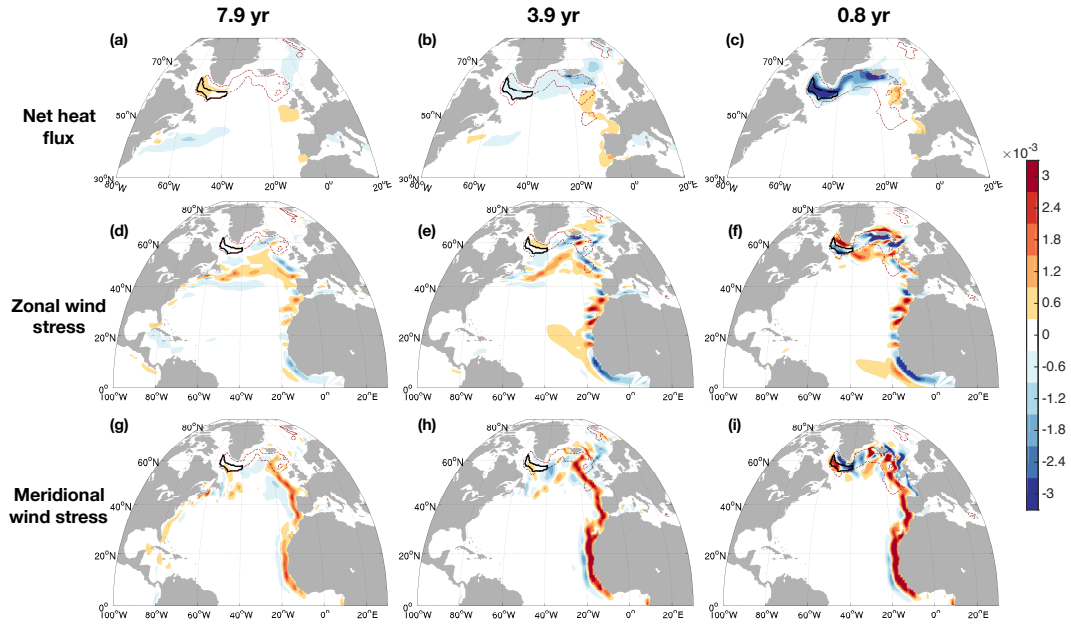
586 In Figure 9(e) and 9(f), we present simplified time series showing the predicted re-
 587 sponse R_{pos} to local (in the Labrador Sea), non-local (everywhere except the Labrador Sea),
 588 and global perturbations (the sum of local and non-local). The non-local kinematic sensi-
 589 tivity exceeds the local kinematic sensitivity for lags longer than about 1 month, but as dis-
 590 cussed above, the local sensitivity decays somewhat slowly with lag, remaining above 10%
 591 of the maximum global value for all lags considered. The global kinematic sensitivity also
 592 decays with lag, described empirically on the interval $[-10,0]$ by two-term exponential de-
 593 cay with timescales $\tau_1 = 8.4$ yr and $\tau_2 = 22$ yr. For dynamic sensitivities (Figure 9), the
 594 predicted response to non-local density anomalies is always positive and larger in magnitude
 595 than the negative response to local density anomalies, thus the global response is always pos-
 596 itive.

597 **3.4 Sensitivity to surface forcing**

598 The heat content of the Labrador Sea can be affected by local and remote surface fluxes,
 599 such as zonal and meridional wind stress and net heat flux. In Figure 10, we examine the 14-
 600 day mean sensitivity fields associated with these processes at the sea surface. Since our nu-
 601 merical model is an ocean-only model with imposed atmospheric forcing, sensitivities are
 602 relative to the imposed surface forcing, as opposed to a dynamic air-sea coupling. Ensem-
 603 ble standard deviations (Figure S5) and animations of the sensitivity fields are available as
 604 supplemental information (Movies S5 through S7).

611 **3.4.1 Net heat flux**

612 By convention, a positive heat flux *decreases* ocean temperature, i.e. ocean heat *loss*
 613 is positive. Large, negative sensitivities in the Labrador Sea at short lags thus indicate, as
 614 one would expect, that local heat gain increases heat content at short lags. At 3.9 year lag,
 615 the largest negative sensitivities are found south of Iceland and in the Nordic Seas (Figure
 616 10). Anomalies in this region can get advected via the subpolar gyre into the LS. There is
 617 also a region of positive sensitivity along the European continental shelf. At 7.9 year lag, the
 618 sensitivity of Labrador Sea heat content to local heat flux has changed sign to positive val-
 619 ues, indicating that the linear, time-delayed response to a local increase in heat loss is in fact



605 **Figure 10.** Ensemble mean sensitivities of the annual- and column-mean Labrador Sea heat content for
 606 objective function years 2002-2011, shown at three different lags (-7.9 years, -3.9 years, and -0.8 years). The
 607 fields have been scaled as $J_0^{-1}(\partial_x J)\Delta x$, where x is the independent variable and J_0 is the scaling constant
 608 $\rho_0 c_p (2.0^\circ\text{C})$. The result is a dimensionless measure of the predicted response of LS heat content to a positive
 609 perturbation Δx applied at one grid point for two weeks, with $\Delta Q_{net} = 60 \text{ W/m}^2$ and $\Delta\tau_E = \Delta\tau_N = 0.06$
 610 N/m^2 .

620 an *increase* in Labrador Sea heat content. This counterintuitive result is broadly consistent
 621 with a mechanism identified by [Williams *et al.*, 2015], in which increasing the density of
 622 the Labrador Sea (e.g. through increased heat loss) accelerates the overturning and increases
 623 heat convergence in the subpolar gyre. However, these positive sensitivity values are much
 624 smaller than negative sensitivity at lag 0.

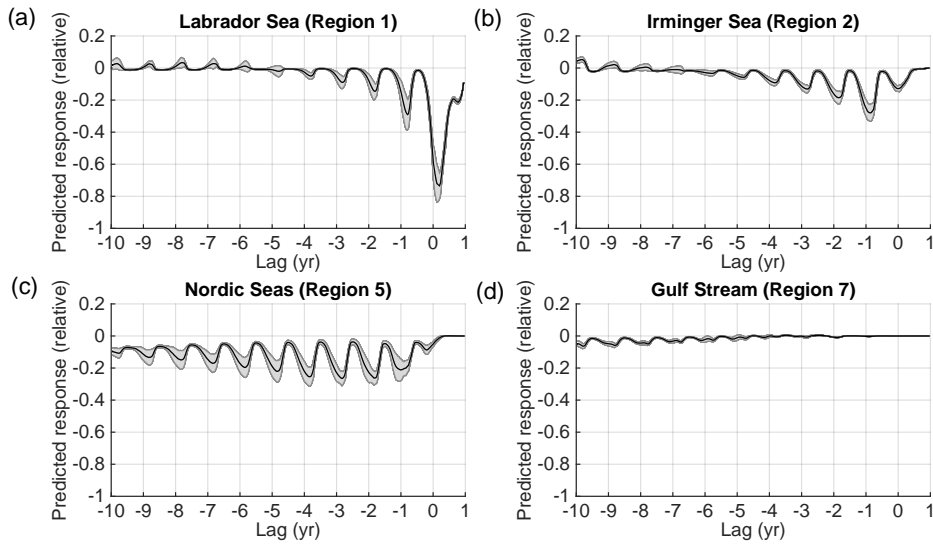
625 For a two-dimensional surface forcing field like net heat flux, the predicted response
 626 metric R_{pos} takes the form:

$$R_{pos,Q}(t) = \sum_{i,j} \left(\frac{\partial J}{\partial x} \right)_{i,j,n} \sigma_Q(\mathbf{r}), \quad (13)$$

627 where $\sigma_Q(\mathbf{r})$ is the two-dimensional, time-independent, deasonalized standard deviation in
 628 net heat flux. The predicted response varies with region and timescale, and an annual cycle is
 629 present in each time series, with extrema in late winter to early spring (see Figure 11).

630 To compare the timing of the predicted response extrema and mixed layer depth, we
 631 construct a mean seasonal cycle for the monthly mean predicted response $R_{pos,Q}$ and mixed
 632 layer depth and calculate various lag correlations between the seasonal cycles. In each region
 633 considered, the monthly mean predicted response leads the monthly mean mixed layer depth
 634 by about one month, so forcing anomalies that occur roughly one month before maximum
 635 mixed layer depth tend to produce the largest linear predicted responses in annual mean LS
 636 heat content. At this lag (-1 month), correlations between predicted responses and mixed
 637 layer depth are very high, explaining over 80% of the variance independently of the region.

638 Considering the full time series again, we see that Labrador Sea heat content is most
 639 sensitive to heat fluxes during the year over which the objective function is defined (Figure
 640 11(a)). The maximum magnitude response occurs at 2.2 ± 0.8 months (positive lag), which
 641 is between February and April in the year over which the objective function is calculated.
 642 Strong vertical mixing over this period enables heat flux anomalies to mix over the largest
 643 possible fraction of the water column, thereby increasing the storage of heat in the relatively
 644 quiescent deep interior Labrador Sea. The heat content is still sensitive to heat fluxes from
 645 the previous 3-4 years, highlighting the importance of preconditioning from previous years in
 646 encouraging deep convection. After roughly 5-7 years, the local sensitivity switches sign, but
 647 it has a much smaller magnitude than the sensitivity to the target year (i.e. the year on the lag
 648 interval [0,1]).



649 **Figure 11.** Predicted response $R_{pos,Q}$ of the Labrador Sea heat content to a uniformly signed perturbation
 650 in the past for the (a) Labrador Sea, (b) Irminger Sea, (c) Nordic Seas, and (d) the Gulf Stream. The objec-
 651 tive function is the annual-and column-mean Labrador Sea heat content for objective function years in the
 652 2002-2011 range. The thick lines indicate ensemble means, and the shading indicates one standard deviation
 653 across the ensemble members. Each sensitivity field has been multiplied by the time-independent, spatially-
 654 varying interannual standard deviation σ_x in the forcing field (Figure S3) and divided by a scaling constant
 655 $J_0 = \rho_0 c_p (2.0^\circ\text{C})$ such that the predicted response is depicted as the non-dimensional form $J_0^{-1}(\partial_x J)\sigma_x(\mathbf{r})$.
 656 The fields are further scaled by the maximum predicted dimensionless response of 1.5×10^{-4} . We use the
 657 convention that positive net heat fluxes *decrease* ocean surface potential temperatures, so a negative predicted
 658 response indicates LS heat loss/gain due to increased/decreased (more positive/negative) air-sea heat flux.

659 The most negative sensitivities to the Irminger sea heat flux occur around lag $-10 \pm$
 660 0.8 months, which is roughly the previous February-March (Figure 11(b)). $R_{pos,Q}$ for the
 661 Irminger Sea is larger than $R_{pos,Q}$ for the Labrador Sea for lags longer than about 10 months.
 662 Sensitivities to fluxes in the broader subpolar gyre (not shown) are non-zero for nearly the
 663 entire 10-year integration period, with decreasing effect each previous year. Sensitivities to
 664 heat fluxes in the Nordic Seas have their greatest magnitudes between lags -4 and -2 years,
 665 although there is considerable spread in the ensemble in winter (Figure 11(c)). Sensitivities
 666 to fluxes in the Gulf Stream region display a complex, double-peaked annual cycle, although
 667 for more negative lags a clearer seasonal signal emerges. By lag -10 years, the Gulf Stream
 668 region predicted responses reach roughly 10% of the local, target year (i.e. between lag 0 and
 669 1) predicted responses to heat fluxes in the Labrador Sea (Figure 11(d)). These results are
 670 broadly consistent with oscillating adjoint sensitivity patterns of the AMOC to changes in the
 671 Labrador Sea region, as reported by *Czeschel et al.* [2010]. Sensitivities to other regions are
 672 small (not shown).

673 **3.4.2 Wind stress**

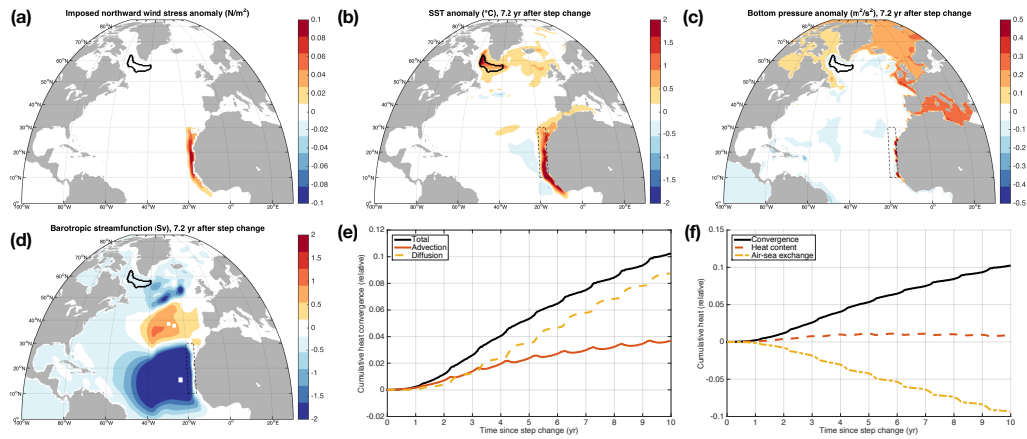
674 Both the zonal and meridional wind stress sensitivity patterns feature numerous posi-
 675 tive/negative sensitivity dipoles (Figure 10). For wind stress, these dipoles indicate regions
 676 where a change in wind position and/or wind stress curl can induce changes in transport
 677 via Ekman pumping/suction. The meridional sensitivity fields feature strong, coastally-
 678 guided, somewhat stationary signals along the eastern edge of the Atlantic basin. Consid-
 679 ering the meridional and zonal sensitivity fields together, we see that the sensitivity pattern
 680 roughly aligns with the local coastline and shelf bathymetry, suggesting that alongshore
 681 winds are important for the predicted response. Although the eastern Atlantic basin is not
 682 a strong source region for the Labrador Sea, changes in these locations can alter dynamics
 683 and heat/salt convergence. This region of positive sensitivity extends from the west coast of
 684 North Africa all the way up to the seas south of Iceland. The adjoint sensitivity fields suggest
 685 that if this region is forced by an increase in northward wind stress, the associated enhanced
 686 coastal downwelling will ultimately induce an *increase* in LS heat and salt content (a positive
 687 anomaly acting on a positive sensitivity region will increase the objective function) and vice
 688 versa.

689 In order to test the hypothesis that an increase in wind stress along the West African
 690 shelf will eventually increase the LS heat content, as suggested by the adjoint model, we

691 perform a 10-year step response experiment using the ECCOv4 setup. After a 10-year spin
692 up under control conditions, we impose a permanent step change in wind stress along the
693 coast with a sign structure that matches the sensitivity field and a maximum magnitude of
694 0.1 N/m^2 (Figure 12(a)). The change in wind stress along the West African shelf induces a
695 change in Ekman transport across the bathymetry that enhances downwelling of warm sur-
696 face waters along the coast, creating an across-bathymetry pressure anomaly.

697 The direct effect of the change in wind stress is largely local, i.e. the warming signal
698 detected in the vicinity of the wind stress perturbation is not connected to the Labrador Sea,
699 as West Africa is not a source region for the Labrador Sea on the timescales considered here
700 (Figure 12(b)). It is instead the across-bathymetry pressure anomaly, which excites a combi-
701 nation of barotropic and baroclinic motions, that ultimately induces a change in Labrador Sea
702 heat content. An initial, rapid bottom pressure anomaly roughly follows f/H contours along
703 the Atlantic side of the Greenland-Iceland-Scotland ridge, reaching the Labrador sea in less
704 than two weeks. In the following 2-3 months, the pressure anomaly makes its way over the
705 Greenland-Iceland-Scotland Ridge, spreading rapidly across the Nordic Seas and the broader
706 Arctic Ocean. The pressure change propagates southwards through the Denmark Strait, set-
707 ting up an across-bathymetry pressure gradient anomaly along the entire northern boundary
708 of the Atlantic Ocean (Figure 12(c)). This basin-wide, across-bathymetry pressure anomaly
709 adjusts for 2-3 years after the step change. The change in basin-scale pressure gradient across
710 the North Atlantic speeds up the circulation of the subpolar gyre (Figure 12(d)). Diffusive
711 heat convergence and advective heat convergence into the LS both increase as the gyre spins
712 up (Figure 12(e)). The net increase in LS heat convergence is strongly offset by an increase
713 in ocean heat loss to the atmosphere, which is likely to encourage convection into the deep
714 ocean and the resulting increase in LS heat storage (Figure 12(f)).

715 The response of the Labrador Sea heat content to this imposed change in wind stress
716 is well approximated by the linear approach used in the adjoint model. We verified this by
717 examining results from four different step response experiments, with maximum values of
718 $\pm 0.1 \text{ N/m}^2$ and $\pm 0.4 \text{ N/m}^2$. For the 0.1 N/m^2 step response, the non-linear component of the
719 response remains small (less than 5% of the maximum linear response for the duration of the
720 model run). For the 0.4 N/m^2 step response experiment, the non-linear component is larger
721 (less than 20% of the maximum linear response). Thus, it appears the linear approximation
722 works well for modest wind stress perturbations, but it starts to break down for large values
723 of wind stress, as one may expect.



724 **Figure 12.** Results of a northward wind stress step response experiment. (a) Spatial pattern of the imposed
 725 change in northward wind stress. Anomalies relative to a control run, 7.2 years after the step change is im-
 726 posed, are shown for (b) sea surface temperature, (c) bottom pressure, and (d) barotropic streamfunction (neg-
 727 ative values indicate counterclockwise rotation). The Labrador Sea region is indicated by a thick black line,
 728 and the approximate region of the wind stress perturbation is shown by a thin dashed line. (e) Time series of
 729 cumulative heat convergence relative to the control run, split into advective and diffusive flux convergence
 730 components. (f) Time series of cumulative heat convergence, cumulative heat exchange with the atmosphere,
 731 and heat storage relative to the control run. Time series (e) and (f) are scaled by the decadal-mean Labrador
 732 Sea heat content, 7.9×10^6 J.

3.4.3 Relative importance of heat flux and wind stress

In order to summarize the complex spatiotemporal information contained in the adjoint sensitivity fields, we use two different formulations of the response function following *Verdy et al.* [2014]. The response of the Labrador Sea heat content to a uniformly-signed perturbation (positive everywhere) in each of the three surface forcing fields is:

$$R_{mean,F}(t) = \left\langle \left\langle \frac{\partial J}{\partial Q_{net}} \sigma_{Q_{net}} \right\rangle \right\rangle + \left\langle \left\langle \frac{\partial J}{\partial \tau_E} \sigma_{\tau_E} \right\rangle \right\rangle + \left\langle \left\langle \frac{\partial J}{\partial \tau_N} \sigma_{\tau_N} \right\rangle \right\rangle, \quad (14)$$

where $\sigma_x = \sigma_x(\mathbf{r})$, the sensitivity fields are functions of space and time, and the angular brackets represent sums of the impacts $(\partial_x J) \sigma_x(\mathbf{r})$ over chosen areas. Each term in equation 14 represents the impact of one particular surface forcing variable, either the net heat flux Q_{net} , eastward wind stress τ_E , or northward wind stress τ_N . In this metric, positive and negative impacts may offset each other in the spatial sum. For example, suppose that net heat flux Q_{net} becomes more positive everywhere in the selected ocean basin. Locations and times with positive sensitivities $\partial_Q J > 0$ contribute to an *increase* in J , whereas locations and times with negative sensitivities $\partial_Q J < 0$ contribute to a *decrease* in J . The metric $R_{mean,F}$ may also be interpreted as the impact of basin-scale changes in forcing [*Verdy et al.*, 2014].

The metric $R_{mean,F}$ represents one extreme on the spectrum of possible responses. The other extreme is the very unlikely case in which the sign of the perturbations exactly match the signs of the sensitivity field, such that the impacts are always positive:

$$R_{var,F}(t) = \left\langle \left\langle \frac{\partial J}{\partial Q_{net}} \sigma_{Q_{net}} \right\rangle \right\rangle + \left\langle \left\langle \frac{\partial J}{\partial \tau_E} \sigma_{\tau_E} \right\rangle \right\rangle + \left\langle \left\langle \frac{\partial J}{\partial \tau_N} \sigma_{\tau_N} \right\rangle \right\rangle, \quad (15)$$

In this metric, there are no cancellations of differently-signed impacts. Locations and times with positive sensitivities contribute to an *increase* in J , and locations and times with negative sensitivities *also* contribute to an *increase* in J . In order for J to respond in this way, the imposed perturbation must have some spatial structure on scales smaller than basin-scale. Note that equation equation 15 is a variant of equation 12, in that equation 15 uses standard deviations for the anomalies and includes multiple terms.

Considered together, the two components of wind stress make a much larger relative contribution to cumulative $R_{var,F}$ (89%) than to $R_{mean,F}$ (49%), highlighting the importance of spatial structure in the wind-driven response of LS heat content (Table 1). Spatially-varying wind forcing that matches the sign structure of the sensitivity fields drives a much larger heat content response than a basin-wide change in wind forcing. This is consistent

771 **Table 1.** Cumulative $R_{mean,F}$ and $R_{var,F}$ for each variable, summed over the entire 11-year duration of the
 772 adjoint sensitivity experiments. Values are displayed as ensemble means and ensemble standard deviations for
 773 each variable, scaled by the total $R_{mean,F}$ and $R_{var,F}$ including all three variables.

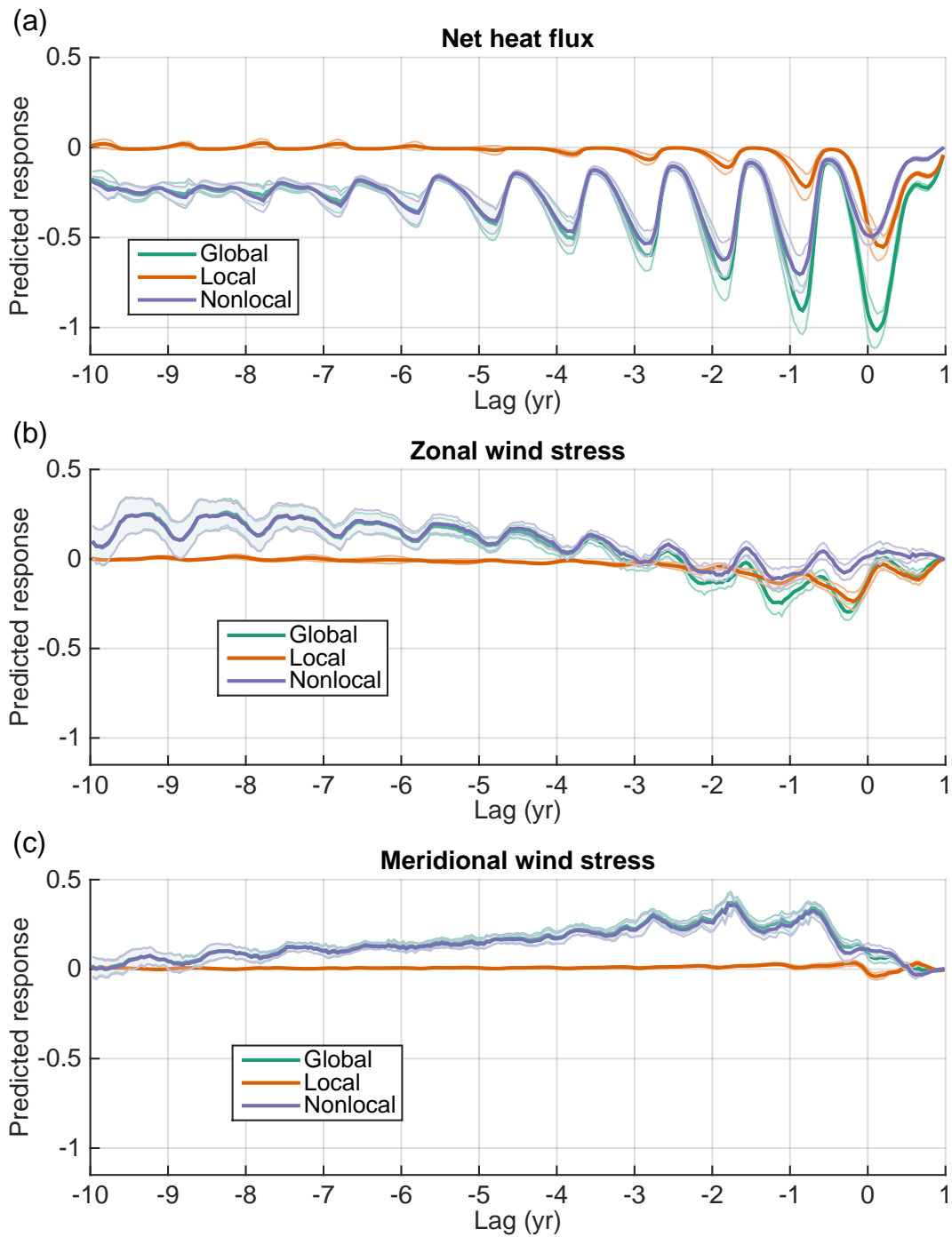
Variable	Cumulative $R_{mean,F}$	Cumulative $R_{var,F}$
Net heat flux	51% \pm 3%	12% \pm 0.3%
Zonal wind stress	25% \pm 6%	47% \pm 1%
Meridional wind stress	24% \pm 2%	41% \pm 1%

762 with the large number of dipoles present in the adjoint sensitivity fields. Under a change in
 763 basin-scale forcing (measured by $R_{mean,F}$), the predicted response from a dipole (with equal
 764 magnitudes) is zero, whereas under a change in forcing that matches the sign structure (meas-
 765 ured by $R_{var,F}$), the response from a dipole is additive. Although the exact partitioning of
 766 the predicted response between zonal wind stress and meridional wind stress is a result of the
 767 decomposition of the wind stress vector into zonal and meridional components, the total pre-
 768 dicted response from the wind stress is independent of the rotation of the wind stress vector.
 769 The ensemble standard deviations for cumulative $R_{mean,F}$ and $R_{var,F}$ are all less than 10%,
 770 so by this measure the sensitivity fields are fairly stationary for years in the range 2002-2011.

774 **3.4.4 Local versus non-local sensitivity to surface forcing**

775 In Figure 13, we quantify the local and non-local contributions of three surface forcing
 776 fields, as well as kinematic and dynamic sensitivities, to the response function $R_{pos,F}$. The
 777 largest response is to net heat flux, particularly to local perturbations in the target year (i.e.
 778 on the lag interval [0,1] yr). In the target year, the predicted response to local forcing is larger
 779 than the predicted response to non-local forcing, but this situation quickly reverses for nega-
 780 tive lags. The responses to zonal and meridional wind stress display a complex range of re-
 781 sponses and timescales, including a strong seasonal cycle and a slow, multi-year adjustment
 782 that reflects the sensitivity of the circulation field to aspects of the wind stress (e.g. gyres
 783 responding to wind stress curl).

791 The cumulative response (summing responses from lag +1 year to more negative lags)
 792 can be used to quantify when cumulative non-local effects exceed cumulative local effects.
 793 This local-to-remote transition timescale t_{LN} offers a simple measure of the relative re-



784 **Figure 13.** Responses $R_{POS,F}$ of the Labrador Sea heat content to local and non-local surface forcing,
 785 scaled by the maximum magnitude response to surface forcing. “Local” is defined as within the Labrador
 786 Sea region shown in Figure 1, and “non-local” is the rest of the global ocean. The sum of the two is denoted
 787 by the response to the “global” forcing. To calculate the response function, the sensitivities are multiplied
 788 by a spatially-varying standard deviation $\sigma_x(\mathbf{r})$ as described in the text and plotted in Figure S3. The lines
 789 indicate ensemble means across 2002-2012, and the shading indicates one standard deviation across ensemble
 790 members. Results are shown relative to the maximum value of the ensemble mean response to net heat flux.

794 sponses of the LS heat content to local and non-local forcing. We estimate the transition
 795 timescale by using cumulative sums of both R_{mean} and R_{var} and report the result as an or-
 796 dered pair (R_{mean} , R_{var}). For net heat flux, the transition timescale is (-0.69,-0.60) yr, which
 797 is 7.2-8.3 months before the start of the objective function integral at lag 0. For lags that are
 798 more negative than (-0.69, -0.60) yr, the cumulative response to non-local changes in net heat
 799 flux exceeds the cumulative response to local changes in net heat flux. There is a sharp dif-
 800 ference between the cumulative response to zonal wind stress and the cumulative response
 801 to meridional wind stress. The transition timescale for meridional (northward) wind stress is
 802 short and positive, (0.9 yr, 1.0 yr), whereas the transition timescale for the zonal (eastward)
 803 wind stress spans a much larger range (-4.8 yr, 1.0 yr). The non-local effect of the merid-
 804 ional wind stress is rapid, dominated by the across-shelf pressure gradient adjustment mech-
 805 anism discussed in section 3.4.2. But the zonal wind stress response contains many positive-
 806 negative dipoles that partially cancel each other when measured by R_{mean} .

807 **4 Conclusions**

808 Using a realistic, observationally-constrained ocean model in adjoint mode [*Forget*
 809 *et al.*, 2015a], we examined the sensitivity of the column-averaged, annual mean heat content
 810 of the Labrador Sea to (1) changes in potential temperature at constant density, (2) changes in
 811 density, and (3) changes in net heat fluxes and wind stresses on 10-year timescales. We pre-
 812 sented key aspects of these complex, temporally- and spatially-varying sensitivity fields and
 813 examined some of the adjustment mechanisms highlighted by the sensitivity fields. By de-
 814 composing the sensitivity fields into kinematic and dynamic components, we tracked poten-
 815 tial source waters for the Labrador Sea and identified both local and remote regions in which
 816 density changes can alter circulation and ultimately change Labrador Sea heat convergence.

817 Positive kinematic sensitivity fields indicate pathways along which potential tempera-
 818 ture changes can affect LS heat content for a fixed circulation pattern. In this way, calculating
 819 positive kinematic sensitivities is conceptually similar to performing "reverse passive tracer
 820 experiments" in which a tracer is allowed to propagate backwards in time following a fixed
 821 pattern of circulation and mixing. In this sense, the kinematic sensitivity fields can also be
 822 thought of as highlighting the "source waters" of the Labrador Sea [*Marotzke et al.*, 1999;
 823 *Song et al.*, 2016]. Our source water calculations indicate that potential Labrador Sea source
 824 regions include the broader subpolar gyre, the Nordic Seas, the North Atlantic Current, and
 825 the Gulf Stream, although the structure of the sensitivity patterns changes considerably with

826 depth and timescale. The difference in the areal extent of the sensitivity fields reflects differ-
827 ences in circulation, e.g. the influence of perturbations spreads more rapidly in the upper 500
828 m of the North Atlantic than at 2000 m.

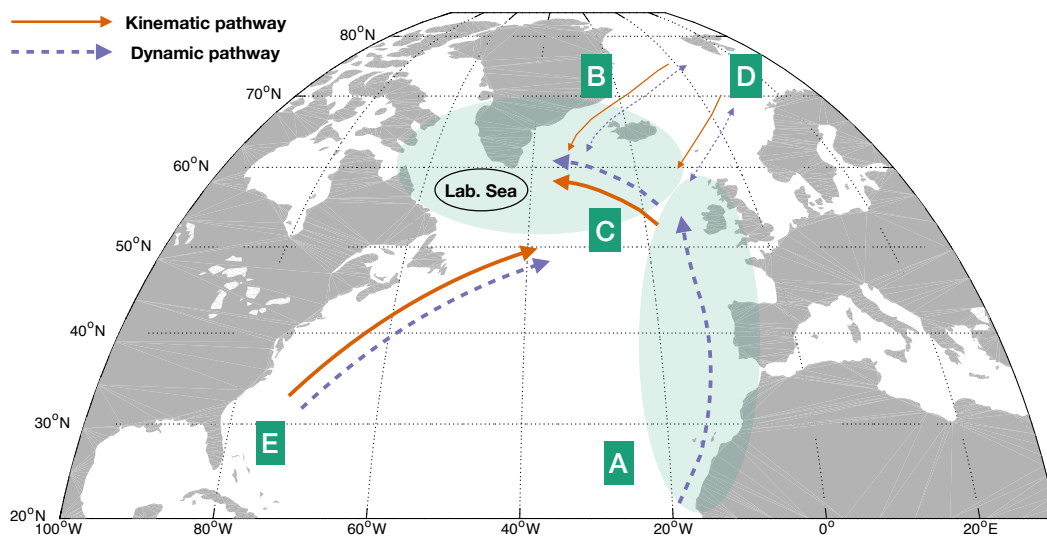
829 By contrast, dynamic sensitivities indicate the linear perturbations that will result in
830 the largest possible changes in LS heat content via changes in density, the associated wave
831 field, and circulation. In the upper 100 m, we find mostly negative sensitivities in the sub-
832 polar gyre, indicating that an increase in upper ocean temperature can *reduce* the depth-
833 averaged heat content by decreasing surface density. In the interior ocean, we find negative-
834 positive dipoles in dynamic sensitivity that are coincident with regions of high kinematic
835 sensitivity, indicating an underlying sensitivity to changes in the across-streamline tilt of den-
836 sity surfaces and the associated geostrophic transport. For example, cooling the Labrador
837 Sea will ultimately *increase* LS heat content via a change in Gulf Stream heat transport and
838 LS heat convergence. This is consistent with a heat convergence adjustment mechanism
839 identified in historical temperature and salinity data as well as in idealized numerical experi-
840 ments [Klöwer *et al.*, 2014; Williams *et al.*, 2015].

841 We also find relatively large dynamic sensitivities along the coast/shelf system of West
842 Africa and Western Europe. This region of dynamic sensitivity is *not* a source region for
843 the LS, i.e. kinematic sensitivities in this region are negligibly small. A similar pattern is
844 also found in the sensitivity to meridional wind stress, indicating an adjustment mode re-
845 lated to changes in pressure. Perturbations in near-coastal, along-bathymetry wind stress in-
846 duce cross-shelf pressure gradients by Ekman transport, and the resulting pressure anomalies
847 propagate northwards along the shelf. This mechanism eventually alters the pressure on the
848 shelf all along the North Atlantic and into the Arctic Ocean, resulting in a change in subpolar
849 gyre circulation and an associated increase/decrease in Labrador Sea heat convergence [Bell,
850 2011, and references therein]. A similar adjustment pathway has been documented for Arc-
851 tic Ocean bottom pressure, albeit for much faster barotropic Kelvin waves [Fukumori *et al.*,
852 2015].

853 In terms of surface forcing, LS heat content is most sensitive to local (in space and
854 time) heat fluxes, though other non-local locations/lags make significant contributions to
855 the predicted response, highlighting the importance of preconditioning and advection of up-
856 stream temperature anomalies. Wind stress sensitivity patterns largely reinforce the pressure

857 wave adjustment mechanism discussed above, as they feature significant positive alongshore
 858 sensitivities.

859 In Figure 14, we summarize some of the dominant adjoint adjustment pathways re-
 860 vealed by the sensitivity fields. On short (less than 1 year) timescales, Labrador Sea heat
 861 content is most sensitive to perturbations in the Labrador Sea, Irminger Sea, the Greenland
 862 coast/shelf, and the eastern boundary of the Atlantic Ocean via pressure gradient adjust-
 863 ments (pathways A and B, Figure 14). On longer timescales, the LS becomes most sensi-
 864 tive to perturbations in the NAC and the Nordic Seas (pathways C and D). On the longest
 865 timescales considered in this study (5-10 years), we find increasingly large sensitivities in the
 866 Gulf Stream region, mainly in the top 500 m (pathway E). Although Figure 14 is a simplified
 867 representation, it provides a clear conceptual framework for understanding the adjustment
 868 pathways of LS heat content.



869 **Figure 14.** Schematic of major kinematic (solid red arrows) and dynamic (dashed green arrows) adjustment
 870 pathways for annual mean Labrador Sea heat content. The pathways include (A) adjustment along the eastern
 871 boundary of the North Atlantic Ocean (dynamic only), which can affect the basin-wide pressure gradient and
 872 the associated circulation, (B) the coastal circulation of the East Greenland Current, (C) the circulation of
 873 the subpolar gyre, (D) exchanges with the Nordic Seas over the Greenland-Iceland-Scotland Ridge, and (E)
 874 circulation of the Gulf Stream and North Atlantic Current. The light green shading indicates regions that can
 875 affect LS heat content on timescales shorter than roughly one year. Changes in the unshaded regions will take
 876 longer than one year to affect LS heat content.

5 Discussion

The sensitivity fields presented in this work can be used to guide further studies on the adjustment of the Labrador Sea to (1) temperature/salinity/density changes and (2) surface forcing perturbations, in part by highlighting optimal locations/times for non-linear forward perturbation experiments. The decomposition of sensitivity fields into kinematic and dynamic components may highlight especially rich areas for future study. For instance, if a unit perturbation in potential temperature is applied just north of the core of the NAC kinematic sensitivities, at a depth of 477 m and a lag of roughly 8 years (see Figure 7 and 8), then the kinematic and dynamic effects would partially cancel each other. In a region of positive kinematic sensitivity, an increase in potential temperature will ultimately get advected into the LS and increase its heat content. However, in a region of negative dynamic sensitivity, an increase in potential temperature will induce a change in density that ultimately decreases LS heat content. The ratio of the kinematic and dynamic responses would depend on how the perturbation is applied, but nevertheless, the presence of opposing kinematic and dynamic sensitivities highlight the presence of potentially complex adjustment mechanisms.

Although we have not explicitly considered the Atlantic Meridional Overturning Circulation (AMOC) in this study, our results may be relevant for understanding connections between the AMOC and Labrador Sea. Deep convection in the LS connects the upper and lower branches of the AMOC, linking the warm, near-surface, northward-flowing waters of the upper branch with the relatively cold, deep, southward-flowing waters of the lower branch [Schmitz and McCartney, 1993; Talley, 2013; Buckley and Marshall, 2016]. Many studies have examined the sensitivity of the Meridional Overturning Circulation to changes in surface forcing [Köhl, 2005; Sévellec *et al.*, 2017]. For example, in a coupled ocean-atmosphere adjoint model, Bugnion *et al.* [2006] detected high sensitivities of the MOC to air-sea heat flux in the Labrador Sea. Czeschel *et al.* [2010] report oscillating sensitivities of the AMOC to net heat flux in the Labrador Sea using an ocean-only model. The sensitivity pattern features a strong seasonal cycle and an increasing sensitivity maximum over a 10-year period. Pillar *et al.* [2016] found that local wind forcing dominates AMOC sensitivity at 27°N on short timescales (in consistency with Evans *et al.* [2017]), while buoyancy (heat and freshwater) fluxes dominates on decadal timescales. Pillar *et al.* [2016] also find sensitivity to meridional wind stress over the West African shelf, in consistency with our suggestion that wind stress perturbations in this region affect the across-slope pressure gradient over the entire North Atlantic, thereby altering large-scale gyre circulation and transport. As the MOC

910 and LS heat content are related but not identical, further work is needed to understand how
911 the MOC results relate to the LS sensitivities presented here. Adjoint sensitivity experiments
912 in higher resolution models, covering longer time periods, and coupled ocean-atmosphere
913 configurations would provide a natural extension to this body of work.

914 Overturning rates in the subpolar gyre are related to the formation and outflow of a
915 cold, fresh, and weakly stratified (i.e. low potential vorticity) mid-depth water mass known
916 as Labrador Sea Water (LSW) [Lazier, 1973; McCartney and Talley, 1982; Talley and Mc-
917 Cartney, 1982; McCartney, 1992; Smethie Jr. et al., 2000]. Maximum overturning occurs in
918 the spring as the newly formed LSW spreads southwards [Holte and Straneo, 2017]. LSW
919 is the lightest component of the North Atlantic Deep Water (NADW), and it is characterized
920 by high concentrations of dissolved oxygen and transient tracers (e.g. anthropogenic carbon,
921 chlorofluorocarbons) [Sy et al., 1997; Steinfeldt et al., 2009; Yashayaev and Loder, 2016].
922 The multi-annual to decadal variability in the AMOC is connected to the variability in LSW
923 formation and thus is relevant for regional and global climate [Robson et al., 2016; Rhein
924 et al., 2017, and references therein]. Labrador Sea Water also connects the subpolar gyre to
925 the broader North Atlantic via the Deep Western Boundary Current (DWBC), either through
926 direct formation of LSW in the DWBC, eddy fluxes of LSW into the DWBC, and advec-
927 tion by a convergent mean flow [Palter et al., 2008; Haine et al., 2008; Hodson and Sutton,
928 2012]. Dynamically, the potential vorticity signature of Labrador Sea Water is connected to
929 the stability of the entire Gulf Stream system, as the stratification of the LSW can affect the
930 amplitude of internal oscillations in the DWBC system [Spall, 1996]. It may be instructive
931 for future adjoint sensitivity studies to use the mean heat/salt content of the entire Labrador
932 Sea Water system as an objective function.

933 We have shown that adjoint sensitivity fields can be used to highlight and quantify po-
934 tential adjustment pathways for heat content in a region of deep convection. We also exam-
935 ined the relative impact of net heat flux and wind stress on LS heat content. These sensitiv-
936 ity estimates can be used to inform future non-linear forward perturbation experiments in
937 both ocean-only and coupled models, which allow for a more thorough investigation of the
938 mechanisms involved in each response pathway. In addition, the adjoint sensitivity fields
939 presented here may also be used to inform the design of future observational networks [He-
940 imbach et al., 2011]. For instance, LS heat content is sensitive to net wintertime air-sea heat
941 fluxes in the Irminger Sea and Nordic Seas over 10-year timescales, so long-term monitoring
942 of fluxes and hydrography in these regions is needed to understand and predict the behavior

943 of the Labrador Sea. Monitoring of wind stress along the West African and European shelf
944 may also be important for projecting LS behavior, as it has an impact on the basin-scale pres-
945 sure gradient of the entire ocean basin. Our results highlight the numerous processes that
946 control the climatically important heat content and the associated heat uptake in a critical
947 region of the North Atlantic Ocean.

948 **Acronyms**

949 **AMOC** Atlantic Meridional Overturning Circulation

950 **DWBC** Deep Western Boundary Current

951 **ECCOv4-r2** Estimating the Circulation and Climate of the Ocean (version 4, release 2)

952 **LS** Labrador Sea

953 **LSW** Labrador Sea Water

954 **MITgcm** Massachusetts Institute of Technology general circulation model

955 **NAC** North Atlantic Current

956 **NADW** North Atlantic Deep Water

957 **MAM** March-April-May time period

958 **TAF** Transformation of Algorithms in Fortran (by FastOpt GmbH)

959 **Acknowledgments**

960 This study is supported by grants from the Natural Environment Research Council
961 (NERC), including [1] The North Atlantic Climate System Integrated Study (ACSIS) [grant
962 NE/N018028/1 (authors DJ, ES) and NE/N018044/1 (authors BS, SJ)], [2] Securing Multi-
963 disciplinary UndeRstanding and Prediction of Hiatus and Surge events (SMURPHS) [grant
964 NE/N006038/1 (author EB) and NE/N005686/1 (authors BS, SJ)], and [3] Ocean Regula-
965 tion of Climate by Heat and Carbon Sequestration and Transports (ORCHESTRA) [grant
966 NE/N018095/1 (authors EB, AM)]. GF is supported by NASA award #1553749 and Si-
967 mons Foundation award #549931. The ECCOv4-r2 model setup used in this work is avail-
968 able for download on Github (https://github.com/gaelforget/ECCO_v4_r2) as an
969 instance of the MIT general circulation model (MITgcm, <http://mitgcm.org/>). Numer-
970 ical model runs were carried out on ARCHER, the UK national HPC facility [[http://](http://archer.ac.uk/)
971 archer.ac.uk/]. Adjoint code was generated using the TAF software tool, created and

972 maintained by FastOpt GmbH [<http://www.fastopt.com/>]. Argo float data is available
973 via <http://www.argo.ucsd.edu/>. The authors wish to thank Ric Williams, Chris Wilson,
974 Yavor Kostov, Maike Sonnewald, Mike Bell, Florian Sevellec, and Nora Loose for conversa-
975 tions that greatly improved the quality of this paper.

976 **References**

- 977 Adcroft, A., and J.-M. Campin (2004), Rescaled height coordinates for accurate representa-
978 tion of free-surface flows in ocean circulation models, *Ocean Modelling*, 7(3-4), 269–284,
979 doi:10.1016/j.ocemod.2003.09.003.
- 980 Adcroft, A., J.-M. Campin, C. Hill, and J. Marshall (2004), Implementation of an Atmo-
981 sphere–Ocean General Circulation Model on the Expanded Spherical Cube, *Monthly*
982 *Weather Review*, 132(12), 2845–2863, doi:10.1175/mwr2823.1.
- 983 Bell, M. J. (2011), Ocean circulations driven by meridional density gradients, *Geophys-
984 ical and Astrophysical Fluid Dynamics*, 105(2-3), 182–212, doi:10.1080/03091929.2010.
985 534468.
- 986 Buckley, M. W., and J. Marshall (2016), Observations, inferences, and mechanisms of the
987 Atlantic Meridional Overturning Circulation: A review, *Reviews of Geophysics*, 54(1),
988 5–63, doi:10.1002/2015RG000493.
- 989 Buckley, M. W., R. M. Ponte, G. Forget, and P. Heimbach (2014), Low-Frequency SST and
990 Upper-Ocean Heat Content Variability in the North Atlantic, *Journal of Climate*, 27(13),
991 4996–5018, doi:10.1175/jcli-d-13-00316.1.
- 992 Bugnion, V., C. Hill, and P. H. Stone (2006), An Adjoint Analysis of the Meridional Over-
993 turning Circulation in a Hybrid Coupled Model, *Journal of Climate*, 19(15), 3751–3767,
994 doi:10.1175/jcli3821.1.
- 995 Campin, J.-M., A. Adcroft, C. Hill, and J. Marshall (2004), Conservation of properties in
996 a free-surface model, *Ocean Modelling*, 6(3-4), 221–244, doi:10.1016/S1463-5003(03)
997 00009-X.
- 998 Campin, J.-M., J. Marshall, and D. Ferreira (2008), Sea ice–ocean coupling using a rescaled
999 vertical coordinate z^* , *Ocean Modelling*, 24(1-2), 1–14, doi:10.1016/j.ocemod.2008.05.
1000 005.
- 1001 Chen, X., and K.-K. Tung (2014), Varying planetary heat sink led to global-warming slow-
1002 down and acceleration, *Science*, 345(6199), 897–903, doi:10.1126/science.1254937.

- 1003 Curry, R. G., M. S. McCartney, and T. M. Joyce (1998), Oceanic transport of subpo-
1004 lar climate signals to mid-depth subtropical waters, *Nature*, *391*(6667), 575–577, doi:
1005 10.1038/35356.
- 1006 Czeschel, L., D. P. Marshall, and H. Johnson (2010), Oscillatory sensitivity of Atlantic
1007 overturning to high-latitude forcing, *Geophysical Research Letters*, *37*(L10601), doi:
1008 10.1029/2010GL043177.
- 1009 Dee, D. P., S. M. Uppala, A. J. Simmons, P. Berrisford, P. Poli, S. Kobayashi, U. Andrae,
1010 M. A. Balmaseda, G. Balsamo, P. Bauer, P. Bechtold, A. C. M. Beljaars, L. van de Berg,
1011 J. Bidlot, N. Bormann, C. Delsol, R. Dragani, M. Fuentes, A. J. Geer, L. Haimberger,
1012 S. B. Healy, H. Hersbach, E. V. Hólm, L. Isaksen, P. Kállberg, M. Köhler, M. Matricardi,
1013 A. P. McNally, B. M. Monge Sanz, J. J. Morcrette, B. K. Park, C. Peubey, P. de Rosnay,
1014 C. Tavolato, J. N. Thépaut, and F. Vitart (2011), The ERA-Interim reanalysis: configu-
1015 ration and performance of the data assimilation system, *Quarterly Journal of the Royal*
1016 *Meteorological Society*, *137*(656), 553–597, doi:10.1002/qj.828.
- 1017 Drijfhout, S. S., A. T. Blaker, S. A. Josey, A. J. G. Nurser, B. Sinha, and M. A. Balmaseda
1018 (2014), Surface warming hiatus caused by increased heat uptake across multiple ocean
1019 basins, *Geophysical Research Letters*, *41*(22), 7868–7874, doi:10.1002/2014GL061456.
- 1020 Evans, D. G., J. Toole, G. Forget, J. D. Zika, A. C. Naveira-Garabato, A. J. G. Nurser, and
1021 L. Yu (2017), Recent wind-driven variability in Atlantic water mass distribution and
1022 meridional overturning circulation, *Journal of Physical Oceanography*, pp. JPO–D–16–
1023 0089.1–39, doi:10.1175/JPO-D-16-0089.1.
- 1024 Fekete, B. M., C. J. Vörösmarty, and W. Grabs (2002), High-resolution fields of global runoff
1025 combining observed river discharge and simulated water balances, *Global Biogeochemical*
1026 *Cycles*, *16*(3), 15–1–15–10, doi:10.1029/1999GB001254.
- 1027 Forget, G., and R. M. Ponte (2015), The partition of regional sea level variability, *Progress*
1028 *in Oceanography*, *137*, 173–195, doi:10.1016/j.pocean.2015.06.002.
- 1029 Forget, G., J. M. Campin, P. Heimbach, C. N. Hill, R. M. Ponte, and C. Wunsch (2015a),
1030 ECCO version 4: an integrated framework for non-linear inverse modeling and global
1031 ocean state estimation, *Geoscientific Model Development*, *8*(10), 3071–3104, doi:
1032 10.5194/gmd-8-3071-2015.
- 1033 Forget, G., D. Ferreira, and X. Liang (2015b), On the observability of turbulent transport
1034 rates by Argo: supporting evidence from an inversion experiment, *Ocean Science*, *11*(5),
1035 839–853, doi:10.5194/os-11-839-2015.

- 1036 Fukumori, I., D. Menemenlis, and T. Lee (2007), A Near-Uniform Basin-Wide Sea Level
1037 Fluctuation of the Mediterranean Sea, *Journal of Physical Oceanography*, 37(2), 338–358,
1038 doi:10.1175/JPO3016.1.
- 1039 Fukumori, I., O. Wang, W. Llovel, I. Fenty, and G. Forget (2015), A near-uniform fluctuation
1040 of ocean bottom pressure and sea level across the deep ocean basins of the Arctic Ocean
1041 and the Nordic Seas, *Progress in Oceanography*, 134(C), 152–172, doi:10.1016/j.pocean.
1042 2015.01.013.
- 1043 Gaspar, P., Y. Grégoris, and J. M. Lefevre (1990), A simple eddy kinetic energy model for
1044 simulations of the oceanic vertical mixing: Tests at station Papa and long-term upper
1045 ocean study site, *Journal of Geophysical Research: Atmospheres*, 95(C9), 16,179–16,193,
1046 doi:10.1029/JC095iC09p16179.
- 1047 Gent, P. R., and J. C. McWilliams (1990), Isopycnal Mixing in Ocean Circulation Mod-
1048 els, *Journal of Physical Oceanography*, 20(1), 150–155, doi:10.1175/1520-0485(1990)
1049 020<0150:imiocm>2.0.co;2.
- 1050 Giering, R., and T. Kaminski (1998), Recipes for adjoint code construction, *ACM Transac-*
1051 *tions on Mathematical Software (TOMS)*, 24(4), 437–474, doi:10.1145/293686.293695.
- 1052 Griewank, A., and A. Walther (2012), *Evaluating Derivatives*, Principles and Techniques of
1053 Algorithmic Differentiation, Second Edition, second ed., Society for Industrial and Ap-
1054 plied Mathematics, doi:10.1137/1.9780898717761.
- 1055 Haine, T., C. Böning, P. Brandt, J. Fischer, A. Funk, D. Kieke, E. Kvaleberg, M. Rhein,
1056 and M. Visbeck (2008), North Atlantic Deep Water Formation in the Labrador Sea,
1057 Recirculation Through the Subpolar Gyre, and Discharge to the Subtropics, in *Arc-*
1058 *tic–Subarctic Ocean Fluxes*, pp. 653–701, Springer Netherlands, Dordrecht, doi:10.1007/
1059 978-1-4020-6774-7_28.
- 1060 Heimbach, P. (2008), *The MITgcm/ECCO adjoint modelling infrastructure*, vol. 13, CLIVAR
1061 Exchanges.
- 1062 Heimbach, P., C. Wunsch, R. M. Ponte, G. Forget, C. Hill, and J. Utke (2011), Timescales
1063 and regions of the sensitivity of Atlantic meridional volume and heat transport Toward
1064 observing system design, *Deep Sea Research Part II*, 58(17-18), 1858–1879, doi:10.1016/
1065 j.dsr2.2010.10.065.
- 1066 Hodson, D. L. R., and R. T. Sutton (2012), The impact of resolution on the adjustment and
1067 decadal variability of the Atlantic meridional overturning circulation in a coupled climate
1068 model, *Climate Dynamics*, 39(12), 3057–3073, doi:10.1007/s00382-012-1309-0.

- 1069 Holte, J., and F. Straneo (2017), Seasonal Overturning of the Labrador Sea as Observed
 1070 by Argo Floats, *Journal of Physical Oceanography*, 47(10), 2531–2543, doi:10.1175/
 1071 jpo-d-17-0051.1.
- 1072 Kieke, D., and I. Yashayaev (2015), Studies of Labrador Sea Water formation and variability
 1073 in the subpolar North Atlantic in the light of international partnership and collaboration,
 1074 *Progress in Oceanography*, 132(C), 220–232, doi:10.1016/j.pocean.2014.12.010.
- 1075 Klöwer, M., M. Latif, H. Ding, R. J. Greatbatch, and W. Park (2014), Atlantic meridional
 1076 overturning circulation and the prediction of North Atlantic sea surface temperature, *Earth
 1077 and Planetary Science Letters*, 406(C), 1–6, doi:10.1016/j.epsl.2014.09.001.
- 1078 Köhl, A. (2005), Anomalies of Meridional Overturning: Mechanisms in the North Atlantic,
 1079 *Journal of Physical Oceanography*, 35(8), 1455–1472, doi:10.1175/JPO2767.1.
- 1080 Large, W., and S. Yeager (2009), The global climatology of an interannually varying air–sea
 1081 flux data set, *Climate Dynamics*, 33, 341–364, doi:10.1007/s00382-008-0441-3.
- 1082 Latif, M., and N. S. Keenlyside (2011), A perspective on decadal climate variability and
 1083 predictability, *Deep Sea Research Part II: Topical Studies in Oceanography*, 58(17-18),
 1084 1880–1894, doi:10.1016/j.dsr2.2010.10.066.
- 1085 Lazier, J., R. Hendry, A. Clarke, I. Yashayaev, and P. Rhines (2002), Convection and restrat-
 1086 ification in the Labrador Sea, 1990–2000, *Deep Sea Research Part I*, 49(10), 1819–1835,
 1087 doi:10.1016/S0967-0637(02)00064-X.
- 1088 Lazier, J. R. N. (1973), The renewal of Labrador sea water, *Deep Sea Research*, 20(4), 341–
 1089 353, doi:10.1016/0011-7471(73)90058-2.
- 1090 Liu, Z., and M. Alexander (2007), Atmospheric bridge, oceanic tunnel, and global climatic
 1091 teleconnections, *Reviews of Geophysics*, 45(2), 1769, doi:10.1029/2005RG000172.
- 1092 Losch, M., D. Menemenlis, J.-M. Campin, P. Heimbach, and C. Hill (2010), On the formula-
 1093 tion of sea-ice models. Part 1: Effects of different solver implementations and parameteri-
 1094 zations, *Ocean Modelling*, 33(1-2), 129–144, doi:10.1016/j.ocemod.2009.12.008.
- 1095 Lozier, M. S., S. Bacon, A. S. Bower, S. A. Cunningham, M. F. de Jong, L. de Steur, B. deY-
 1096 ounge, J. Fischer, S. F. Gary, B. J. W. Greenan, P. Heimbach, N. P. Holliday, L. Houpert,
 1097 M. E. Inall, W. E. Johns, H. L. Johnson, J. Karstensen, F. Li, X. Lin, N. Mackay, D. P.
 1098 Marshall, H. Mercier, P. G. Myers, R. S. Pickart, H. R. Pillar, F. Straneo, V. Thierry,
 1099 R. A. Weller, R. G. Williams, C. Wilson, J. Yang, J. Zhao, and J. D. Zika (2017), Over-
 1100 turning in the Subpolar North Atlantic Program: A New International Ocean Observ-
 1101 ing System, *Bulletin of the American Meteorological Society*, 98(4), 737–752, doi:

- 1102 10.1175/bams-d-16-0057.1.
- 1103 Marotzke, J., R. Giering, K. Q. Zhang, D. Stammer, C. Hill, and T. Lee (1999), Construc-
 1104 tion of the adjoint MIT ocean general circulation model and application to Atlantic heat
 1105 transport sensitivity, *Journal of Geophysical Research: Atmospheres*, *104*(C12), 29,529–
 1106 29,547, doi:10.1029/1999JC900236.
- 1107 Marshall, J., C. Hill, L. Perelman, and A. Adcroft (1997), Hydrostatic, quasi-hydrostatic, and
 1108 nonhydrostatic ocean modeling, *Journal of Geophysical Research*, *102*(C3), 5733–5752.
- 1109 Mazloff, M., P. Heimbach, and C. Wunsch (2010), An Eddy-Permitting Southern Ocean
 1110 State Estimate, *Journal of Physical Oceanography*, *40*, 880–899.
- 1111 McCartney, M. S. (1992), Recirculating components to the deep boundary current of
 1112 the northern North Atlantic, *Progress in Oceanography*, *29*, 283–383, doi:10.1016/
 1113 0079-6611(92)90006-L.
- 1114 McCartney, M. S., and L. D. Talley (1982), The Subpolar Mode Water of the North Atlantic
 1115 Ocean, *Journal of Physical Oceanography*, *12*, 1169–1188, doi:10.1175/1520-0485(1982)
 1116 012<1169:TSMWOT>2.0.CO;2.
- 1117 McDougall, T., and P. Barker (2011), Getting started with TEOS-10 and the Gibbs Seawater
 1118 (GSW) Oceanographic Toolbox, *SCOR/IAPSO WG127*.
- 1119 Ortega, P. (2017), Mechanisms of decadal variability in the Labrador Sea and the wider
 1120 North Atlantic in a high-resolution climate model, *Climate Dynamics*, *49*(7), 2625–2647,
 1121 doi:10.1007/s00382-016-3467-y.
- 1122 Palter, J. B., M. S. Lozier, and K. L. Lavender (2008), How Does Labrador Sea Water Enter
 1123 the Deep Western Boundary Current?, *Journal of Physical Oceanography*, *38*(5), 968–
 1124 983, doi:10.1175/2007jpo3807.1.
- 1125 Pérez, F. F., H. Mercier, M. Vázquez-Rodríguez, P. Lherminier, A. Velo, P. C. Pardo,
 1126 G. Rosón, and A. F. Rios (2013), Atlantic Ocean CO₂ uptake reduced by weaken-
 1127 ing of the meridional overturning circulation, *Nature Geoscience*, *6*(2), 146–152, doi:
 1128 10.1038/ngeo1680.
- 1129 Pickart, R. S., F. Straneo, and G. W. K. Moore (2003), Is Labrador Sea Water formed in the
 1130 Irminger basin?, *Deep Sea Research Part I*, *50*(1), 23–52, doi:10.1016/s0967-0637(02)
 1131 00134-6.
- 1132 Pillar, H. R., P. Heimbach, H. L. Johnson, and D. P. Marshall (2016), Dynamical Attribution
 1133 of Recent Variability in Atlantic Overturning, *Journal of Climate*, *29*(9), 3339–3352, doi:
 1134 10.1175/JCLI-D-15-0727.1.

- 1135 Piron, A., V. Thierry, H. Mercier, and G. Caniaux (2017), Gyre-scale deep convection in the
1136 subpolar north atlantic ocean during winter 2014-2015, *Geophysical Research Letters*,
1137 *44*(3), 1439–1447, doi:10.1002/2016gl071895.
- 1138 Rayner, N. A., D. E. Parker, E. B. Horton, C. K. Folland, L. V. Alexander, D. P. Rowell, E. C.
1139 Kent, and A. Kaplan (2003), Global analyses of sea surface temperature, sea ice, and night
1140 marine air temperature since the late nineteenth century, *Journal of Geophysical Research:*
1141 *Atmospheres*, *108*(D14), 14, doi:10.1029/2002JD002670.
- 1142 Rhein, M., R. Steinfeldt, D. Kieke, I. Stendardo, and I. Yashayaev (2017), Ventilation vari-
1143 ability of Labrador Sea Water and its impact on oxygen and anthropogenic carbon: a re-
1144 view, *Philosophical Transactions of the Royal Society A: Mathematical, Physical and En-*
1145 *gineering Sciences*, *375*(2102), 20160,321, doi:10.1098/rsta.2016.0321.
- 1146 Robson, J., R. Sutton, K. Lohmann, D. Smith, and M. D. Palmer (2012), Causes of the Rapid
1147 Warming of the North Atlantic Ocean in the Mid-1990s, *Journal of Climate*, *25*(12),
1148 4116–4134, doi:10.1175/jcli-d-11-00443.1.
- 1149 Robson, J., D. Hodson, E. Hawkins, and R. Sutton (2014), Atlantic overturning in decline?,
1150 *Nature Geoscience*, *7*(1), 2–3, doi:10.1038/ngeo2050.
- 1151 Robson, J., P. Ortega, and R. Sutton (2016), A reversal of climatic trends in the North At-
1152 lantic since 2005, *Nature Geoscience*, *9*(7), 513–517, doi:10.1038/ngeo2727.
- 1153 Roemmich, D., and J. Gilson (2009), The 2004-2008 mean and annual cycle of tempera-
1154 ture, salinity, and steric height in the global ocean from the Argo Program, *Progress in*
1155 *Oceanography*, *82*, 81–100, doi:10.1016/j.pocean.2009.03.004.
- 1156 Schmitz, W. J., and M. S. McCartney (1993), On the North Atlantic Circulation, *Reviews of*
1157 *Geophysics*, *31*, 29–49, doi:10.1029/92RG02583.
- 1158 Sévellec, F., and A. V. Fedorov (2017), Predictability and Decadal Variability of the North
1159 Atlantic Ocean State Evaluated from a Realistic Ocean Model, *Journal of Climate*, *30*(2),
1160 477–498, doi:10.1175/jcli-d-16-0323.1.
- 1161 Sévellec, F., A. V. Fedorov, and W. Liu (2017), Arctic sea-ice decline weakens the Atlantic
1162 Meridional Overturning Circulation, *Nature Climate Change*, *7*(8), 604–610, doi:10.1038/
1163 nclimate3353.
- 1164 Smethie Jr., W. M., R. A. Fine, A. Putzka, and E. P. Jones (2000), Tracing the flow of North
1165 Atlantic Deep Water using chlorofluorocarbons, *Journal of Geophysical Research-Oceans*,
1166 *105*(C6), 14,297–14,323, doi:10.1029/1999JC900274.

- 1167 Song, H., J. Marshall, M. J. Follows, S. Dutkiewicz, and G. Forget (2016), Source waters for
1168 the highly productive Patagonian shelf in the southwestern Atlantic, *Journal of Marine*
1169 *Systems*, 158(C), 120–128, doi:10.1016/j.jmarsys.2016.02.009.
- 1170 Spall, M. A. (1996), Dynamics of the Gulf Stream/Deep Western Boundary Current
1171 Crossover. Part II: Low-Frequency Internal Oscillations, *Journal of Physical Oceanog-*
1172 *raphy*, 26, 2169–2182, doi:10.1175/1520-0485(1996)026<2169:DOTGSW>2.0.CO;2.
- 1173 Spall, M. A. (2004), Boundary Currents and Watermass Transformation in Marginal Seas*,
1174 *Journal of Physical Oceanography*, 34(5), 1197–1213, doi:10.1175/1520-0485(2004)
1175 034<1197:bcawti>2.0.co;2.
- 1176 Steinfeldt, R., M. Rhein, J. L. Bullister, and T. Tanhua (2009), Inventory changes in anthro-
1177 pogenic carbon from 1997-2003 in the Atlantic Ocean between 20°S and 65°N, *Global*
1178 *Biogeochemical Cycles*, 23(3), n/a–n/a, doi:10.1029/2008GB003311.
- 1179 Sutton, R. T., G. D. McCarthy, J. Robson, B. Sinha, A. Archibald, and L. J. Gray (2017), At-
1180 lantic Multi-decadal Variability and the UK ACSIS programme, *Bulletin of the American*
1181 *Meteorological Society*, doi:10.1175/BAMS-D-16-0266.1.
- 1182 Sy, A., M. Rhein, J. R. N. Lazier, K. P. Koltermann, J. Meincke, A. Putzka, and M. Bersch
1183 (1997), Surprisingly rapid spreading of newly formed intermediate waters across the North
1184 Atlantic Ocean, *Nature*, 386(6626), 675–679, doi:10.1038/386675a0.
- 1185 Talley, L. (2013), Closure of the Global Overturning Circulation Through the Indian, Pacific,
1186 and Southern Oceans: Schematics and Transports, *Oceanography*, 26(1), 80–97, doi:10.
1187 5670/oceanog.2013.07.
- 1188 Talley, L. D., and M. S. McCartney (1982), Distribution and Circulation of Labrador
1189 Sea Water, *Journal of Physical Oceanography*, 12(11), 1189–1205, doi:10.1175/
1190 1520-0485(1982)012<1189:dacols>2.0.co;2.
- 1191 Thacker, W. C., and R. B. Long (1988), Fitting dynamics to data, *Journal of Geophysical*
1192 *Research*, 93(C2), 1227–1240, doi:10.1029/JC093iC02p01227.
- 1193 Vage, K., R. S. Pickart, V. Thierry, G. Reverdin, C. M. Lee, B. Petrie, T. A. Agnew, A. Wong,
1194 and M. H. Ribergaard (2008), Surprising return of deep convection to the subpolar North
1195 Atlantic Ocean in winter 2007–2008, *Nature Geoscience*, 2(1), 67–72, doi:10.1038/
1196 ngeo382.
- 1197 Verdy, A., M. R. Mazloff, B. D. Cornuelle, and S. Y. Kim (2014), Wind-Driven Sea Level
1198 Variability on the California Coast: An Adjoint Sensitivity Analysis, *Journal of Physical*
1199 *Oceanography*, 44(1), 297–318, doi:10.1175/JPO-D-13-018.1.

- 1200 Watkins, M. M., D. N. Wiese, D.-N. Yuan, C. Boening, and F. W. Landerer (2015), Improved
1201 methods for observing Earth's time variable mass distribution with GRACE using spheri-
1202 cal cap mascons, *Journal of Geophysical Research: Solid Earth*, *120*(4), 2648–2671, doi:
1203 10.1002/2014JB011547.
- 1204 Williams, R. G., V. Roussenov, M. S. Lozier, and D. Smith (2015), Mechanisms of Heat
1205 Content and Thermocline Change in the Subtropical and Subpolar North Atlantic, *Jour-
1206 nal of Climate*, *28*(24), 9803–9815, doi:10.1175/JCLI-D-15-0097.1.
- 1207 Wunsch, C. (2009), *Discrete Inverse and State Estimation Problems*, Cambridge University
1208 Press, Cambridge, doi:10.1017/CBO9780511535949.
- 1209 Yashayaev, I., and J. W. Loder (2009), Enhanced production of Labrador Sea Water in 2008,
1210 *Geophysical Research Letters*, *36*(1), 1764, doi:10.1029/2008gl036162.
- 1211 Yashayaev, I., and J. W. Loder (2016), Recurrent replenishment of Labrador Sea Water and
1212 associated decadal-scale variability, *Journal of Geophysical Research-Oceans*, *121*(11),
1213 8095–8114, doi:10.1002/2016JC012046.
- 1214 Yashayaev, I., and J. W. Loder (2017), Further intensification of deep convection in the
1215 Labrador Sea in 2016, *Geophysical Research Letters*, doi:10.1002/2016GL071668.